Effect of dielectric barrier discharge plasma actuators on vortical structures in a mixing layer

Srikar Yadala, Nicolas Benard, Marios Kotsonis, Eric Moreau

Physics of Fluids

Effect of dielectric barrier discharge plasma actuators on vortical structures in a mixing layer

Srikar Yadala,[1, 2] Nicolas Benard,[1, a)] Marios Kotsonis,[2] and Eric Moreau[1]

[1)] *Institut PPRIME, Université de Poitiers (CNRS UPR 3346, ISAE-ENSMA), Boulevard Marie et Pierre Curie, BP 30179, 86962 Futuroscope, France*

[2)] *AWEP Department, Section of Aerodynamics, Delft University of Technology, Kluyverweg 1, 2629HS Delft, The Netherlands*

(Dated: 30 November 2020)

The influence of spanwise-uniform electro-fluid-dynamic (EFD) forcing applied by a dielectric barrier discharge (DBD) plasma actuator on the growth of a plane mixing layer and the dynamics of large-scale spanwise vortices, are investigated experimentally. A two-dimensional mixing layer formed between two streams of air with different velocities is employed for this study. Quantitative spatio-temporal measurement of the flow field is acquired using high-speed planar particle image velocimetry. The DBD actuator was constructed such that it imparts perturbations into the splitter-plate boundary layer formed by the high-velocity fluid stream, close to the trailing edge. Through this, the fundamental Kelvin-Helmholtz (KH) instability of the current mixing layer and its first sub-harmonic are forced. Forcing the fundamental instability results in the inhibition of vortex pairing due to the attenuation of sub-harmonic instabilities and thus, mixing layer growth is halted in the vicinity of the trailing edge. With sub-harmonic instability forcing, neighbouring vortices interact with each other and amalgamate together through mutual induction. This results in a higher growth rate compared to the unforced mixing layer at the streamwise location of this vortex interaction. Eventually, the growth rate of the forced mixing layers become similar to that of the unforced case. These results demonstrate the influence of the applied forcing on the spectral signature, growth and stability characteristics of the plane mixing layer, and the dynamics of the coherent vortical structures.

[a)] The author to whom correspondence may be addressed: nicolas.benard@univ-poitiers.fr

I. INTRODUCTION

The interaction of two parallel streams of different free-stream velocity gives rise, at the trailing-edge of a splitter plate, to a plane mixing layer. In such flow conditions, the shear region at the interface of the fluid streams is responsible for turbulent energy production. A notable observation from Brown and Roshko [1] is the development of of organised, large-scale, spanwise (coherent) vortices. The mixing layer flow field is unstable to the perturbations arising from the inviscid Kelvin-Helmholtz (KH) instability mechanism. This leads to an exponential growth of two-dimensional waves (primary instability) downstream of the splitter plate, ultimately resulting in their roll-up into discrete spanwise vortices[2]. The vortical flow structures in the mixing layer are primarily governed by the large-scale effects of the turbulent energy production which can be manipulated by imparting small-amplitude periodic perturbations[3].

The amalgamation of subsequent spanwise vortices, or vortex pairing, has a significant influence on the growth of the mixing layer as demonstrated by Winant and Browand [2]. Sub-harmonic frequencies of the most-amplified (fundamental) KH instability, forming immediately downstream of the splitter plate, act as catalyst to the vortex pairing process and hence influence the growth of the mixing layer[3,4]. The amplification of the sub-harmonic is attributed to *sub-harmonic resonance* which is a consequence of the non-linear interaction between the fundamental instability and its first sub-harmonic[5,6]. Under suitable conditions (mainly favourable phase relation between the two instability waves) this interaction can reinforce the sub-harmonic, resulting in its growth. The fundamental and its sub-harmonic instability waves, influence the relative position and strength of the ensuing vortices and hence regulate the amalgamation process[7,8].

The advantage of applying flow control on the plane mixing layer is twofold. Firstly, it aides in better understanding and ascertaining the dynamics of the turbulent structures generated in the shear layer and hence the transport of turbulent energy through this large-scale motion. Secondly, this flow arrangement governs the rate of mixing in combustion chambers, as well as in jets and wakes. It also forms a major source of broadband noise associated with jet propulsion. Furthermore, flow over modern aircraft wings is dominated by complex interactions between free-shear flows. Thus, devising methods to control the dynamics within and growth of a plane mixing layer can have many practical applications.

A number of control techniques have been employed in previous experimental efforts to control the shear layer instabilities. One method involves the introduction of perturbations into the free-streams at an upstream location[4,9,10]. Introduction of perturbation at the splitter-plate trailing edge directly into the mixing layer flow field, either through an oscillating flap[3] or through acoustic means[8,11] have also demonstrated successful control. Inducing boundary-layer separation close to the splitter-plate trailing edge through steady pneumatic injection was employed by Mathis *et al.*[12] and blowing through nozzles machined at the splitter-plate trailing edge was successfully used for control by Parezanović *et al.*[13]. However, many of these techniques have inherent features affecting the nature of the introduced instabilities. Such as spanwise modulation and strong vertical components in case of suction/blowing synthetic jets[14], a strong vertical component and no frequency (and hence instability) control in the case of forced boundary-layer separation[12], or non-harmonic forcing in terms of distributed heating. Thus arises the need for novel actuation concepts able to initiate the natural instabilities in the shear layer at accurately selected frequencies as well as in a spanwise-uniform manner. Alternating current (AC) dielectric barrier discharge (DBD) plasma actuator is an ideal candidate to meet this necessity and hence is employed in the current study.

DBD plasma actuators work on the principle of air ionisation. The authority of these actuators as a flow control device can be attributed to a volume distributed Coulombian or electro-fluid-dynamic (EFD) body force. This is a result of air ionisation and collision of these ions with neutral air particles in the vicinity, when supplied with an alternating current (AC) signal. A thorough review on the basic principles and working mechanism of these actuators can be found in Benard and Moreau[15]. These actuators have gathered considerable attention as active flow control devices in recent years. They have found many successful boundary layer flow control applications for instability control[16,17] and turbulent drag reduction[18]. In contrast to laminar/transitional and wall-bounded flow configurations, previous work on application of DBD plasma actuators in mixing layers is limited. Ely and Little[19] and Singh and Little[20] compared the effectiveness of momentum-based actuation by AC-DBD plasma actuators with thermal perturbations introduced by nanosecond (ns-) DBD actuators in manipulating the instabilities in a mixing layer and thus affecting its growth. Low-frequency perturbations were imparted into the flow field with both actuators. The acquired results showed that AC-DBD actuators have more control authority over the

mixing layer compared to ns-DBD actuators which resulted in similar flow dynamics when supplied with six times the energy input for an AC-DBD actuator. This is attributed to the higher receptivity of the flow to momentum-based input than thermal perturbations.

In the current research, spanwise-uniform EFD forcing exerted on the mixing layer with an AC-DBD plasma actuator is utilized to excite/amplify the fundamental and sub-harmonic KH instabilities separately (single-frequency excitation). The subsequent effect on the spanwise vortices within the mixing layer and the pairing process is investigated experimentally. The uniqueness of AC-DBD actuator forcing needs to be highlighted here. The EFD forcing exerted does not have a strong vertical component and the imparted perturbation is confined near the dielectric surface. In the current study, this feature is exploited to investigate the impact of exciting different primary KH instabilities in the mixing layer, by imparting well-controlled streamwise perturbations into the splitter-plate boundary layer ensuing on the high-velocity side. Thus the necessary instability control is realized here in an indirect manner, by manipulating the shear and spectral content within the incoming boundary layer. Largely horizontal forcing emulates the effect of boundary layer instabilities (i.e. Tollmien-Schlichting waves) developing upstream of the splitter-plate trailing edge. Thus the chosen forcing technique provides a more "realistic" forcing environment than other techniques and replicates the features of perturbations in the natural case, albeit at a well-controlled frequency and amplitude.

This article is organised as follows: the experimental set-up is introduced in section II. Results pertaining to the unforced mixing layer is presented in section III and the influence of the applied EFD forcing on the mixing layer is discussed in section IV. The conclusions drawn from this study are in section V.

II. EXPERIMENTAL SET-UP

A. Wind-tunnel

The experiments were carried out in a closed-loop wind tunnel with test-section dimensions 30 cm $\times$ 30 cm $\times$ 1.2 m in height, width and length respectively. The wind tunnel was specially modified to accommodate mixing layer studies as shown in figure 1a. To this effect, a 15 mm thick aluminium (splitter) plate extended from the entrance of the settling

chamber, just after the honeycomb, through the convergent and until the entrance of the test section (black line in figure 1a). The aluminium plate split this section of the wind-tunnel into two equal halves along the vertical direction, thereby generating two parallel flow streams. The end of the aluminium plate was attached with a PMMA attachment (see figure 1b) which completed the splitter plate. This attachment had a 120 mm long taper and a 3 mm thick trailing edge. The use of PMMA as the material for this attachment is motivated by its additional application as the dielectric for the DBD plasma actuator. To this effect, a spanwise incision was produced on its bottom side (dark gray area in figure 1b). This incision was made such that 2 mm thick PMMA remained on the top side, which served as the dielectric substrate. The details of the design and construction of the DBD plasma actuator is presented in section II B. The incision was filled with an epoxy resin, before performing surface treatment to obtain a smooth and uninterrupted surface.

One metallic grid (with wire diameter of 0.18 mm and solidity of 35%) was installed just upstream of the convergent in the top flow stream to breakdown the incoming vortices and reduce the free-stream turbulence in this stream. In order to realize a difference in the velocity between the two streams, a combination of foams and a perforated plate was installed just upstream of the convergent, in the bottom stream, to reduce its velocity (black rectangle in figure 1a). A set of four metallic grids (same as in top stream) was installed downstream of the perforated plate to reduce the level of free-stream turbulence in this stream (vertical black lines in figure 1a).

The base-flow configuration selected for this study and used in all cases reported here, was a two-dimensional plane mixing layer formed between two streams of air with free-stream velocities maintained at $U_1 = 5$ m s^{-1} (bottom) and $U_2 = 10$ m s^{-1} (top). The resultant velocity ratio is $r = U_1/U_2 = 0.5$. The velocity difference between the two flow streams is $\Delta U = U_2 - U_1 = 5$ m s^{-1}. The average of the velocities of the two streams, which is expected to be the convection speed of the spanwise vortices in the ensuing mixing layer[21], is $\overline{U} = (U_2 + U_1)/2 = 7.5$ m s^{-1}. With these two velocity parameters, a second velocity ratio is defined as $R = \Delta U/(2\overline{U})$ which in the current experiment is $R = 0.33$. This ratio gives an estimate of the relative magnitude of the total shear (ΔU), when compared to the average velocity of the two streams ($\overline{U}$). Turbulence intensity (Tu) was measured in both streams with a single hot-wire sensor. The turbulence intensity (bandpass filtered between 10 and 1000 Hz) in the low and high-velocity streams are $Tu_1/\overline{U} \approx 0.9\%$ and $Tu_2/\overline{U} \approx 0.3\%$

respectively.

The coordinate system used in this study is represented by (x, y, z) where x is along the free-stream direction, y is perpendicular to the plane of the mixing layer and z is along the span. The corresponding velocity components are represented by u, v and w respectively. The geometrical origin of the mixing layer is fixed at the trailing-edge of the splitter plate (see figure 1b), with $z = 0$ being at the centre of the splitter plate along the span (15 cm from both walls). It is worth noting here that the splitter-plate boundary layers on both the high- and low-velocity sides were not tripped. Measurements of the boundary layers were made with the electrodes of the DBD plasma actuator (especially one on the high-velocity side) having been installed. Both boundary layers were found to be laminar at the end of the splitter plate (boundary layer shape factors being $H_1 \approx 2.8$ and $H_2 \approx 2.9$ at $x = -1$ mm). The momentum thickness of the splitter-plate boundary layer ensuing on the high-velocity side, just upstream of the trailing edge (at $x = -1$ mm) was measured to be $\theta_i = 0.55$ mm. This value is utilized henceforth to non-dimensionalize the spatial coordinates and other length parameters wherever necessary.

B. DBD plasma actuator

The DBD plasma actuator was constructed just before the trailing-edge of the splitter plate, on the PMMA attachment as shown in figure 1b. As mentioned previously, an incision made on the bottom side from $x = -42$ mm to $x = -2$ mm (dark gray area in figure 1b) resulted in a 2 mm thick PMMA plate on the top side which constituted the dielectric substrate for the actuator. Ho and Huang[4] show that the fundamental KH instability in the mixing layer is characterised by the high-velocity boundary layer. This is because, the higher shear contained within this boundary layer has a greater influence on turbulent energy production within the mixing layer and thus, linear instability growth and formation of coherent vortices. Thus, flow control is expected to be more effective if applied in this boundary layer, which was confirmed byEly and Little[19]. Thus, in the current experiment, the air-exposed electrode of the DBD actuator was flush-mounted on the top side of the PMMA attachment. The second electrode was installed inside the incision which was then filled with an epoxy resin to encapsulate the second electrode, thus avoiding any unwanted spark generation between the electrodes.

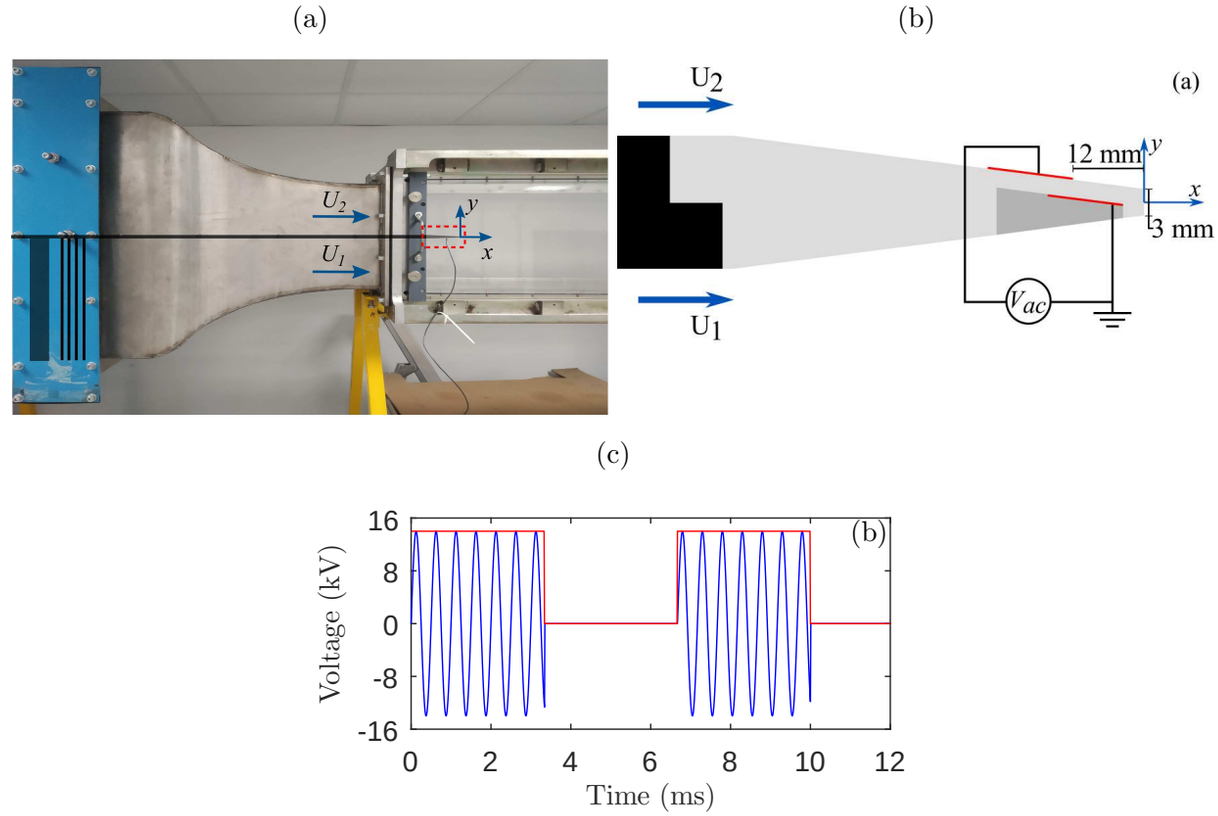

FIG. 1: (a) Wind-tunnel set-up with location of foams and perforated plate (dark rectangle), metallic grids (four vertical lines) and the splitter plate (black: aluminium plate, gray: trailing edge attachment). (b) Splitter-plate trailing edge design (dashed red rectangle in (a), not to scale). Aluminium plate (black), PMMA attachment (light gray), electrodes of the actuator (red lines), the epoxy resin encapsulating the grounded electrode (dark gray) and coordinate system used in this study are depicted. (c) Sample input waveform (blue) and square-wave burst modulation (red) ($V_{ac} = 14$ kV, $f_{ac} = 2$ kHz, $f_b = 150$ Hz).

The electrodes of the DBD plasma actuator were uniform strips of aluminium with a non-reflective black coating (total thickness of 85 μm). The air-exposed electrode was 50 mm wide while the encapsulated electrode was 15 mm wide. The electrodes were mounted asymmetrically, with a relative overlap of 5 mm to ensure consistent plasma generation. This construction resulted in a DBD plasma actuator that exerts a spanwise-uniform EFD force on the boundary layer generated by the high-velocity stream along the free-stream direction at $x = -12$ mm. The EFD forcing is applied along the streamwise direction as the

intention here is to impart fluctuations into the mixing layer flow field in order to amplify certain convective instabilities.

The air-exposed electrode was supplied with the high-voltage AC signal while the encapsulated electrode was grounded. The actuator was powered using a *Trek 30/20A* (±30 kV, 20 mA) high-voltage amplifier. The amplifier applied a gain of 3 kV/V to the input voltage provided by a *Lecroy WaveStation 3082* function generator. For all test-cases with EFD forcing presented here, the AC voltage waveform was sinusoidal with amplitude $V_{ac} = 14$ kV and carrier frequency $f_{ac} = 2$ kHz. Furthermore, a low-frequency burst modulation (square waveform, 50% duty cycle) with a burst frequency f_b, was applied on the input AC signal. A sample of the resulting input signal is depicted in figure 1c. The AC carrier frequency is responsible for the ionisation process and hence the production of the EFD force, while the burst frequency influences the instabilities in the mixing layer.

Performance

The performance of the employed DBD actuator is characterised by measuring the power consumed and the corresponding thrust generated. To this effect, the actuator was operated with a sinusoidal AC waveform with no burst modulation. The power consumed by the actuator was estimated through an integral charge measurement technique for which a monitor capacitor ($C_M = 47$ nF) was connected in series between the encapsulated electrode and the ground[22]. At every tested voltage amplitude, 100 AC cycles were used to converge to an average value of power (P_{avg}) which is presented in figure 2a. Similar to previous research efforts with actuators constructed on thick dielectric substrates[22,23], the acquired results demonstrate that the variation of power consumption with input AC voltage amplitude is well approximated by a curve $P_{avg} = A_P(V_{ac} - V_0)^2$ (dashed red curve in figure 2a). Here, V_0 is the plasma onset voltage amplitude and A_P is a constant coefficient that depends on the dielectric material, electrode geometry, environmental conditions and AC carrier frequency. By fitting a curve (in the least-squares sense) on the data, these parameters were found to be $V_0 = 4$ kV and $A_P = 6.82 \cdot 10^{-8}$ W V^{-2}. It is worth noting that this fitting is only valid after the plasma ignition voltage (V_0). The constant coefficient obtained here is comparable to that reported by Pons, Moreau, and Touchard[22].

The time-averaged, wall-parallel thrust (T_x) produced by this DBD actuator was mea-

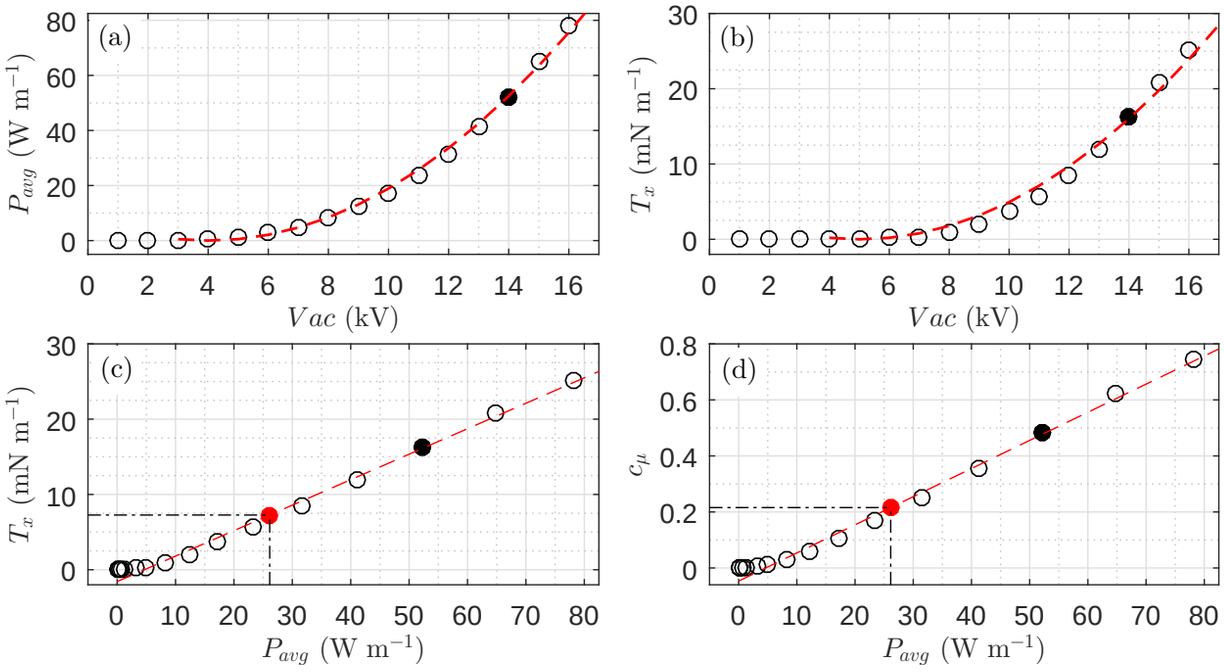

FIG. 2: Performance parameters of the employed DBD plasma actuator ($f_{ac} = 2$ kHz, no burst modulation); (a) and (b) show the average power consumed (P_{avg}) and thrust generated (T_x) respectively, as a function of voltage amplitude (V_{ac}). Thrust generated (T_x) and momentum coefficient (c_μ) versus average power consumed are presented in (c) and (d) respectively. Solid black markers: performance of the actuator at $V_{ac} = 14$ kV. Solid red markers: estimate of the actuator's performance with a low-frequency burst modulation ($V_{ac} = 14$ kV).

sured using a *Denver Instrument SI-603* (0.02 mN precision) laboratory balance. The balance was placed in a Faraday box to prevent any electromagnetic interference. The DBD actuator was fixed vertically such that the induced jet is oriented upwards, so as to measure the force in the wall-parallel direction. Time-averaged thrust was estimated from an ensemble of 1000 samples acquired at a rate of 50 Hz by the balance through a *LabView* interface. The average error in this measurement $\epsilon_{T_x} \approx 1\%$. These results are presented in figure 2b. It is worth noting that the measured values are not the total force generated by the DBD actuator, but the EFD force subtracted by frictional forces incurred due to the presence of the dielectric substrate. Similar to the power consumption, the thrust generated too is well approximated by the relation $T_x \propto (V_{ac} - V_0)^2$ post the plasma ignition voltage as observed by Debien, Benard, and Moreau [24].

The generated thrust is found to be a quasi-linear function of the input power[24], as can be seen from figure 2c. This is expectable as both these parameters are proportional to $(V_{ac} - V_0)^2$. The slope of a linear fit through the data points is 0.34 mN W^{-1} which is an approximation of the effectiveness of the current DBD plasma actuator.

The generated thrust characterizes the actuation in an integrated manner. In order to represent the applied force in non-dimensional terms and to give an estimate of its magnitude relative to the experimental flow field, the momentum coefficient (c_μ) is utilized. This is computed using the measured wall-parallel thrust by:

$$c_\mu = \frac{T_x}{\frac{1}{2}\rho U_2 \cdot \theta_i} \tag{1}$$

Here, ρ (= 1.225 kg m^{-3}) is the density of air and θ_i (= 0.55 mm) is the momentum thickness of the high-velocity side boundary layer close to the splitter-plate trailing edge. Given that the DBD plasma actuator imparts momentum into the splitter-plate boundary layer on the high-velocity side (see figure 1), this free-stream velocity $U_2 = 10$ m s^{-1} is used to compute the momentum coefficient. The variation of the momentum coefficient with the average power consumed is presented in figure 2d.

The average power consumed by the DBD plasma actuator when operated at $V_{ac} = 14$ kV, $f_{ac} = 2$ kHz (AC parameters when EFD forcing is being applied on the mixing layer) is $P_{avg} = 52.2$ W m^{-1} (solid black marker in figure 2a). When the actuator is operated with a burst-modulated AC waveform, the consumed power does not vary with the burst frequency, but depends only on its duty cycle[25,26]. Given the application of a burst modulation with 50% duty cycle on the input AC signal, to manipulate the instabilities in the mixing layer, this value of power can be halved. Thus, the average power consumed by the actuator while applying the necessary EFD force on the mixing layer is $P_{avg,f} = 26.1$ W m^{-1}. However, the same cannot be done to estimate the thrust generated, due to inertial and viscous effects of the flow. Thus, the thrust generated by the actuator is estimated from figure 2c using the power consumption and found to be $T_x = 7.26$ mN m^{-1} (solid red marker). At the present flow conditions and with the measured thrust, the corresponding momentum coefficient is $c_\mu = 0.22$ (solid red marker in figure 2d).

Jolibois and Moreau[27] reported the maximum velocity induced by a DBD actuator with a 2 mm thick PMMA as the dielectric substrate, at different input electric power. Using

the measured power consumption of the DBD actuator at the current operating conditions ($P_{avg,f} = 26.1$ W m^{-1}), the maximum time-averaged velocity in the induced jet is estimated to be $U_f \approx 2.5$ m s^{-1}. The velocity ratio between this velocity of the induced jet and the high-velocity free-stream is then $(U_f/U_2) = 0.25$. Since the momentum of the free-stream is not changing, the momentum coefficient computed previously is representative of this velocity ratio.

C. Particle image velocimetry

Previous experimental studies on the mixing layer flow configuration have mainly employed hot-wire anemometry (HWA), which is a point-field measurement, to obtain the flow velocity. Some more recent studies have made use of planar particle image velocimetry (PIV), however these were mostly not time-resolved[12,13,19,20]. While these studies have contributed a great deal to the current physical understanding of the stability and dynamics of the mixing layer, pertinent features of the flow field remain unresolved due to the inherent limitations of these measurement techniques. These are essentially the functional relationship between the mean flow and development of instabilities in both space and time. The importance of such spatio-temporal information cannot be understated as it has the potential of providing a closure between the topology of the mean flow, its ensuing stability and the development of instabilities such as KH rollers, which in turn affect the mean flow through non-linear interactions such as vortex merging.

To this end, time-resolved planar-PIV was employed for the measurement of the flow field velocity. The experimental set-up is as shown in figure 3. The inspected plane is along the $x - y$ directions, at mid-span ($z = 0$). The flow was seeded with particles of dielectric oil (*Shell Ondina*) injected upstream of the wind-tunnel convergence. A Nd:YAG high speed *Continuum Mesa PIV* laser (18 mJ per pulse) was employed for particle illumination from downstream. The laser head was also placed outside the wind tunnel and the light beam was shaped into a 1 mm thick light sheet. The imaging of the necessary field of view (FOV) was carried out using two *Photron FastCAM SA-Z* cameras featuring a 1024×1024 px^2 CMOS sensor (with 20 μm pixels and 12 bits of digital resolution). Both cameras were installed outside the wind-tunnel test section at about 0.5 m from the measurement plane, which was imaged through an optical window. The cameras were equipped with a *Nikon Nikkor* 50 *mm*

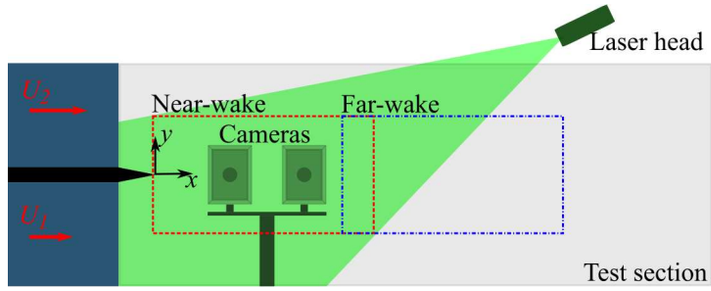

FIG. 3: PIV experimental set-up. The test section, splitter plate, PIV cameras, laser-head and laser sheet are depicted. The free-stream velocities and the coordinate system are also shown. The two captured fields: near-wake (dashed red rectangle) and far-wake (dash-dotted blue rectangle) are also represented.

lens operated at $f_{\#} = 2$. The resulting magnification factor of each camera is $M = 0.12$.

The laser and the two cameras were synchronized using a *Lavision High Speed Controller* and *Lavision Davis 8.4.0* suite. Image acquisition, pre-processing and cross-correlation were performed using the same software package. Cross-correlation was carried out with a final interrogation window of 12×12 px^2 with a relative overlap of 50%. The final vector spacing is 1 mm in both x and y directions. The acquisition rate during all the tested cases was 9.5 kHz in single-frame mode. Thus, the pulse separation between subsequent frames was 105 μs. A sequence of 20000 images were acquired using both the cameras for every tested flow case. The resulting measurement time was 2.1 s per test case.

The two cameras were placed adjacent to each other such that their respective FOVs overlap each other by about 26 mm. A calibration plate was employed to stitch the fields captured by the two cameras using *Lavision Davis 8.4.0* suite which resulted in a final FOV of 318×169 mm^2. This arrangement (2 cameras and laser) was traversed along the streamwise direction to capture two fields. The first field (near-wake, dashed (red) rectangle in figure 3) spanned from just upstream of the splitter-plate trailing-edge to about $x = 305$ mm, while the second field (far-wake, dash-dotted (blue) rectangle in figure 3) spanned from about $x = 280$ mm to $x = 598$ mm. These two fields overlapped each other by about 26 mm as well and were stitched together using the same calibration plate with an in-house *MatLab* script. The size of the resulting FOV was 610×169 mm^2.

The trigger to the PIV system was synchronized with the beginning of a burst modulation cycle ($t = 0$ s in figure 1cb). It is worth noting that for all tested cases, the DBD plasma

actuator was operational for 10 seconds before the start of the PIV acquisition. This was to ensure that the mixing layer had reorganised itself according to the applied EFD forcing before the PIV acquisition.

Correlation error in planar PIV is estimated to be 0.1 pixels[28]. In the current experiment, typical particle displacement was approximately 6 pixels. Thus, the relative error in the measurement of the displacement is of the order of 2%. The relative error on the time separation is very low and can be neglected. Therefore, the relative error of the measured velocity (instantaneous and/or fluctuating fields) is approximated to be $\epsilon_{V(t)} = 2\%$ where $V(t)$ is a time-series of instantaneous velocity fields. The uncertainty on the time-averaged velocity fields is computed using the linear error propagation technique[29]. The uncertainty $\epsilon_{\overline{V}}$ $(= \sigma_{V(t)}/\sqrt{ES})$ of any average velocity field $\overline{V}$ is determined from the standard deviation of the corresponding time-series ($\sigma_{V(t)}$) and the number of samples (ES) that are uncorrelated in time. The maximum uncertainty on the time-average field in the current experiment is $\epsilon_{\overline{u}} \approx 4\%$ and $\epsilon_{\overline{v}} \approx 3\%$.

III. UNFORCED MIXING LAYER

The baseline flow configuration of the ensuing plane mixing layer is discussed here. It is good to note that the DBD plasma actuator was mounted on the splitter plate (figure 1b) but not operational while acquiring the PIV fields for the baseline. Thus, this test case is henceforth referred to as *unforced mixing layer* (UML).

The splitter plate employed for this study has a 3 mm thick trailing edge as discussed in section II B, which results in a wake effect that manifests as the formation of a recirculation region just downstream of the splitter-plate trailing edge. This was also observed by Laizet, Lardeau, and Lamballais[30] who performed direct numerical simulation (DNS) to study the effect of splitter-plate trailing edge shapes on the spatial development of the mixing layer. In the current unforced mixing layer the recirculation region is observed to last until about $x/\theta_i \approx 44$ ($x \approx 24$ mm).

The normalised, time-averaged u-velocity component ($\overline{u}_N$) is presented in figure 4a. The normalisation of the mean field is performed according to equation 2.

$$\overline{u}_N = \frac{\overline{u} - U_1}{\Delta U} \tag{2}$$

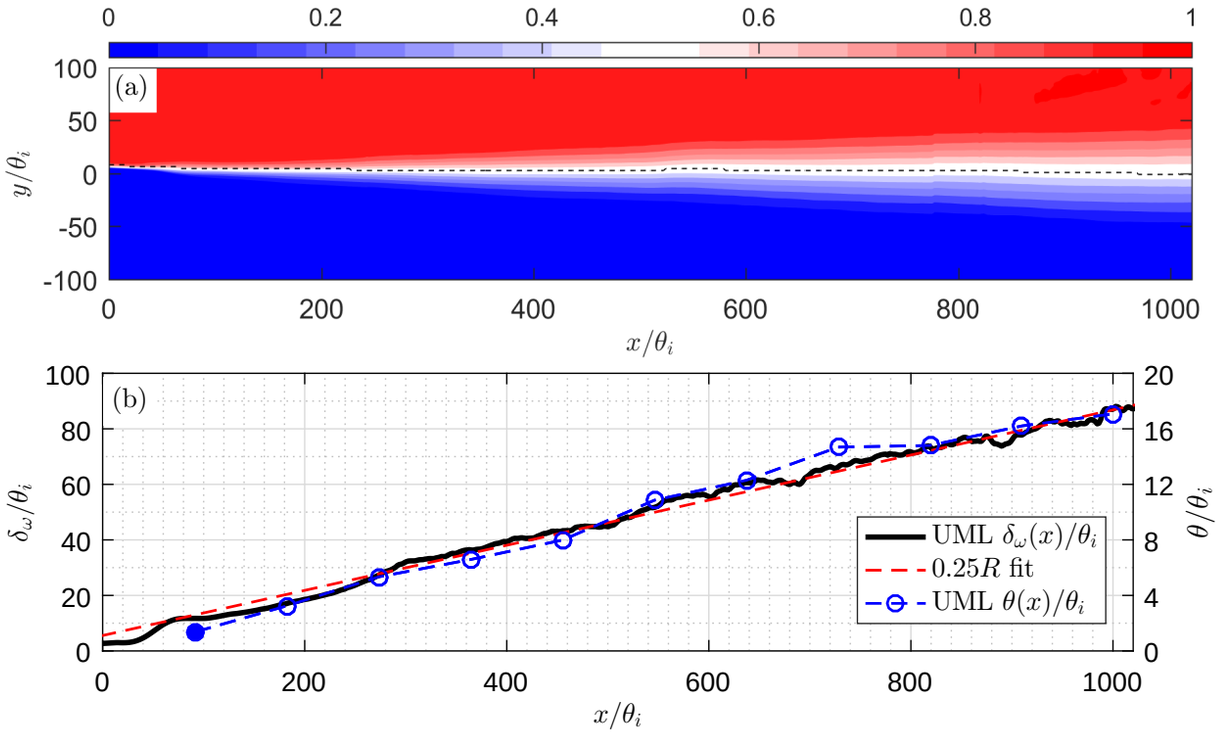

FIG. 4: (a) Time-averaged, normalised u-velocity ($\overline{u}_N$) of the unforced mixing layer. The dashed (black) line represents $y_{0.5}$ trace. (b) Vorticity thickness along the streamwise direction. Also shown is the integral (momentum) thickness at select streamwise stations.

The $\overline{u}_N$ velocity presented in figure 4a contains both the near-wake and far-wake PIV FOVs. The mixing layer developed due to the interaction of the high and low-velocity flow streams, downstream of the splitter-plate trailing edge, is clearly visible. Also shown in this figure is the $y_{0.5}$ trace (dashed black line) which represents the y-coordinate where $\overline{u}_N = 0.5$.

The growth of the mixing layer is quantified with the vorticity thickness (δ_ω). The motivation of using this parameter is that the development of the mixing layer is a product of the unstable motion caused by the vorticity distribution, which manifests itself as large-scale coherent vortices in the flow field[1]. Given that these vortices, by entrainment of irrotational fluid or by amalgamation[2], influence the growth of the mixing layer, it is appropriate to use the vorticity thickness for this purpose. It is computed according to equation 3 given below.

$$\delta_\omega = \frac{\Delta U}{(d\overline{u}/dy)_{max}} = \frac{1}{(d\overline{u}_N/dy)_{max}} \tag{3}$$

The vorticity thickness of the unforced mixing layer along the streamwise direction is presented in figure 4b. Until $x/\theta_i \approx 44$ no growth is observed due to the occurrence of the

recirculation region. A sudden increase in the vorticity thickness is observed just downstream of this location. This pertains to the laminar region where the linear instability causes the roll-up of the shear layer at the fundamental (or naturally preferred) frequency, resulting in the formation of spanwise-oriented vortices[2,31]. This is followed by a linear growth from $x/\theta_i \approx 100$ which can be attributed to vortex pairing occurring stochastically in space and time as previously observed[2–4]. It is also noteworthy that the growth pattern of the current mixing layer resembles that of the mixing layer ensuing from a thin trailing edge in the numerical work of Laizet, Lardeau, and Lamballais[30].

The spreading rate of the mixing layer can be approximated by the Abramovich[32]-Sabin[33] rule given by $d\delta_\omega/dx = c \cdot R$, where the constant c is a fitting parameter. In the linear growth region of the current mixing layer, the overall spreading rate is well approximated by $d\delta_\omega/dx = 0.25 \cdot R$ (dashed red line in figure 4b). The value of the fitting parameter $c = 0.25$ is greater compared to the generally accepted range of $c = 0.16$ to 0.18[1]. The increase in spreading rate can be attributed to the higher level of free-stream turbulence in the low velocity stream, which results in an increased entrainment and hence, growth rate[34]. However, the complex interaction of the splitter-plate wake with the mixing layer cannot be neglected either. The fitting parameter of the current mixing layer is similar to that observed in the experiments Huang and Ho[11] (approximated to be 0.27).

Also shown in figure 4b is the mixing layer integral thickness (often referred to as momentum thickness θ) computed by equation 4.

$$\theta = \int_{-\infty}^{\infty} \frac{\overline{u} - U_1}{\Delta U} \cdot \left[1 - \frac{\overline{u} - U_1}{\Delta U}\right] dy \tag{4}$$

In the turbulent region of the current unforced mixing layer, the integral thickness too increases linearly along the streamwise direction. The growth rate measured corresponding to the integral thickness is $d\theta/dx \approx 0.017$. This growth rate is comparable to that observed by Ho and Huang[4] ($d\theta/dx \approx 0.013$) in their mixing layer with a velocity ratio ($R = 0.31$) similar to the current study.

Self-preservation or self similarity implies that the flow field is in a state of dynamic equilibrium and is not affected by the initial conditions any more[35]. The necessary conditions to ascertain that the mixing layer has achieved self-similarity are that the growth is linear and the mean and fluctuating quantity profiles become geometrically similar along the downstream direction when scaled with the velocity difference and plotted along a non-

dimensional (similarity) coordinate[36,37]. Profiles of the normalised mean streamwise velocity ($\overline{u}_N$) at different streamwise locations are shown in figure 5a. A non-linear least-square-fit of the $\overline{u}_N$-velocity on to the hyperbolic-tangent profile ($U_{tanh} = 0.5 \cdot [1 + tanh(y)]$) was carried out and this fit is also shown in the figure (black curve). It is worth noting that the y-coordinate in this plot (and in figure 5b) is shifted with the location of $y_{0.5}$ at the particular streamwise location and is non-dimensionalised with the local vorticity thickness ($\delta_\omega(x)$).

The wake effect of the thick splitter-plate trailing edge manifests itself as a velocity defect in these profiles[37,38]. While the recirculation region lasts until $x/\theta_i \approx 44$, a velocity defect is observed downstream of this location (see profile at $x/\theta_i = 60$). Thus, the wake effect extends beyond the recirculation region, shifting the location where self-similarity is achieved further downstream[38]. The mean velocity profiles downstream of $x/\theta_i = 130$ collapse on to each other (and the *tanh* profile) well, suggesting the absence of the splitter-plate wake effect. Furthermore, the mixing layer has a linear growth downstream of this location as well (as observed in figure 4b) which suggests that with respect to the mean flow quantities, the current mixing layer achieves self-similarity at $x/\theta_i = 130$.

However, as observed in previous works[36,37], the turbulent properties become self-similar further downstream. Profiles of the Reynold's shear stress (R_{xy}), non-dimensionalised with $(\Delta U)^2$, at different streamwise locations are presented in figure 5b. Similar to the observations of Braud *et al.*[38] with a thick splitter-plate trailing edge, in the region where the wake effect is significant, the profiles of the Reynold's stress contain two extrema as a result of the velocity defect caused by the wake (see profile at $x/\theta_i = 60$). The high-velocity side has a positive extremum while the low-velocity side contains a comparatively smaller negative extremum (more pronounced further upstream). The negative extremum decreases along the stream and disappears after $x/\theta_i = 130$, indicating the decrease in the influence of the splitter-plate wake. Once the wake effect is overcome, the Reynold's stress profiles have a classical bell-shape with just one maxima within the mixing layer[3,11,36,38].

The variation of maximum Reynold's stress value along the streamwise direction is presented in figure 5c. As a consequence of the stitching of the near-wake and far-wake PIV FOVs, the computed values between $x/\theta_i = 510$ and 550 (dotted red line) are not reliable and hence are not shown. Initially, a significant peak is observed owing to the splitter-plate wake. This is also observable through figure 5b where the maximum Reynold's stress in the

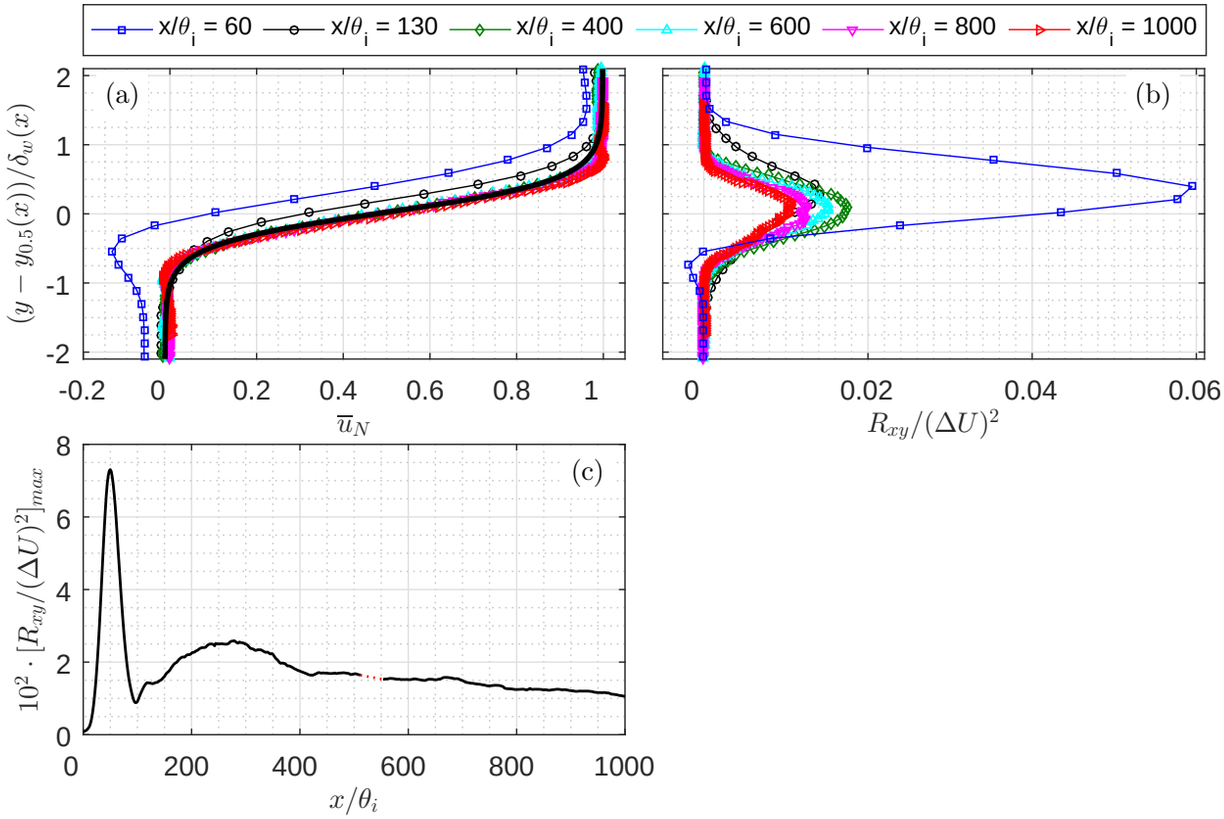

FIG. 5: (a) Profiles of $\overline{u}_N$-velocity at different streamwise locations and the *tanh* fit (thick black curve) on profile at $x/\theta_i = 600$. (b) Profiles of Reynold's shear stress ($R_{xy} = -\overline{u'v'}$) at different streamwise locations non-dimensionalised with $(\Delta U)^2$. (c) Maximum value of R_{xy} along the streamwise direction. Red dotted line represents region of PIV frame stitching.

profile at $x/\theta_i = 60$ is significantly higher than the others. Post this, the maximum value gradually increases until $x/\theta_i \approx 270$ and then starts to reduce. It reaches a constant value at $x/\theta_i \approx 400$ and remains so until $x/\theta_i \approx 700$. Downstream of $x/\theta_i = 700$, the maximum Reynolds shear stress is observed to decrease (as also seen in the profiles at $x/\theta_i = 800$ and 1000). Following these observations, it is estimated that the current unforced mixing layer does not attain self-similarity with respect to fluctuating parameters within the measured domain.

As mentioned previously, the characteristic spanwise vortices that exist in a mixing layer arise from the inviscid KH instability. The subsequent amalgamation of these vortices depend on the presence and strength of sub-harmonic instability waves of the most-amplified

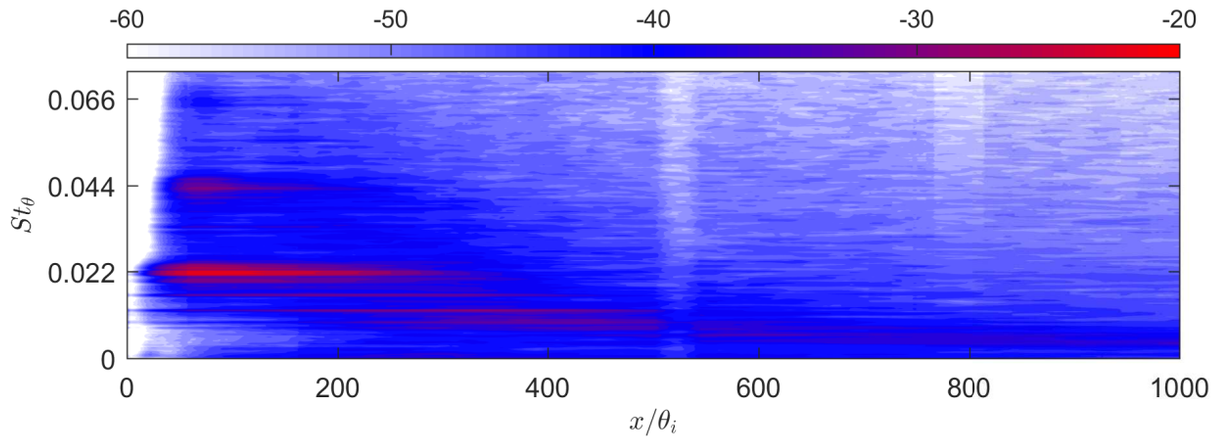

FIG. 6: Non-dimensional, normalised power spectra ($\Phi_N^{v'} \cdot \Delta f/\overline{U}^2$ (dB), $\Delta f = 5$ Hz) of the v'-velocity component sampled along the $y_{0.5}$- line in figure 4a.

(or fundamental) KH instability forming immediately downstream of the splitter-plate trailing edge[4,7,8]. Thus, knowing the frequency of the fundamental KH instability is absolutely necessary. One method to determine this is to measure the passage frequency of the spanwise vortices initially, which will correspond to the frequency of the fundamental instability[4]. To this effect, time-series of the fluctuations of the transversal velocity component (v') sampled along the $y_{0.5}$ line in the unforced mixing layer (dashed (black) line in figure 4a) are analysed in the Fourier domain. The power spectra are computed using Welch's method with a final frequency resolution of $\Delta f = 5$ Hz. The spectra are normalized by equation 5 (in agreement with Parseval's theorem),

$$\Phi_N^{v'} \cdot \Delta f = (\Phi^{v'} \cdot \Delta f) \frac{\frac{1}{ES-1}\sum_t (v')^2}{\sum_f (\Phi^{v'} \cdot \Delta f)} \tag{5}$$

where Φ is the computed power spectral density (PSD) and ES is the temporal ensemble size. The summations are performed with respect to the corresponding subscript. The power spectra are non-dimensionalised with $\overline{U}^2$.

The computed power spectra is shown in figure 6. Here, the vertical access denotes the vortex passage frequency. This is represented in non-dimensional form as the Strouhal number $St_\theta = f\theta_i/\overline{U}$, where θ_i and $\overline{U}$ are the momentum thickness of the high-velocity boundary layer and the average velocity of the two streams. Fluctuations with highest energy correspond to $St_\theta = 0.022$ (frequency band of 300 ± 10 Hz). These are observed to be strongest close to the splitter plate and reduces downstream, becoming comparatively

low for $x/\theta_i > 350$. Thus, the fundamental KH instability in the current flow configuration is expected to have a Strouhal number of $St_0 = 0.022$ ($f_0 = 300$ Hz). The corresponding wavelength of the fundamental instability wave is λ_0/θ_i ($= \overline{U}/f_0\theta_i$) $= 45.5$ ($\lambda_0 = 25$ mm). The Strouhal number computed with the local integral momentum thickness at $x/\theta_i = 91$ (solid blue marker in figure 4b) is $f_0\theta(x)/\overline{U} = 0.03$ which corroborates well with linear stability theory. Given the manifestation of the recirculation region up to $x/\theta_i \approx 44$ in the current set-up, this comparison is carried out approximately one instability wavelength after the disappearance of this recirculation region, as suggested by Ho and Huerre[39]. Finally, following the work of Michalke[31], if the free-stream velocity of the high-velocity stream (U_2) is used as the characteristic velocity to compute the Strouhal number of the fundamental KH instability, it is found to be ($f_0\theta_i/U_2 =$) 0.017 which corroborates well with their computation.

Fluctuations at the harmonic of the fundamental instability band ($St_\theta = 2 \cdot St_0 = 0.044$) are also observed. However they contain lesser energy and occur in a smaller region along the streamwise direction. Fluctuations are also observed around $St_\theta = 0.011$ ($f = 150$ Hz) which is in the frequency band about the first sub-harmonic of the fundamental KH instability ($St_0/2$). The onset of these fluctuations are downstream compared to the fundamental instability, as expected. Additionally they become strongest at $x/\theta_i \approx 350$ which is approximately the location where the fluctuations of the fundamental instability are observed to become very weak. Fluctuations at $St_\theta = 0.016$ ($f = 220$ Hz) are seen to co-exist with the fundamental instability, although with less energy. However, the energy of these fluctuations maximise further downstream at $x/\theta_i \approx 200$.

IV. PRIMARY INSTABILITY FORCING

The instability modes that will be forced by the DBD plasma actuator with the burst frequency (f_b) are chosen based on the observations of the power spectra computed on the unforced mixing layer. Therefore, EFD forcing at $c_\mu = 0.22$ was applied to impart perturbations pertaining to the fundamental KH instability $St_f = St_0 = 0.022$ ($f_b = 300$ Hz) and its first sub-harmonic, $St_f = St_0/2 = 0.011$ ($f_b = 150$ Hz). The effect of this spanwise-uniform EFD forcing on the mixing layer is discussed here.

The evolution of vorticity thickness (equation 3) along the streamwise direction for the

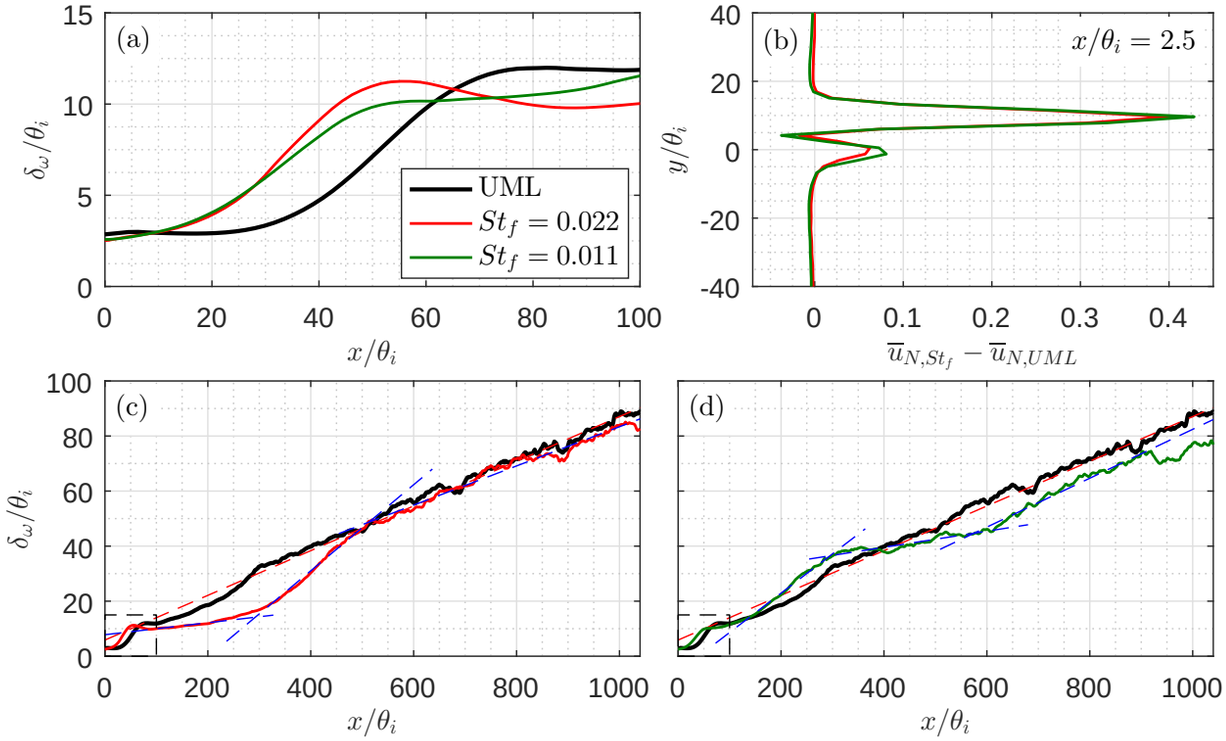

FIG. 7: Vorticity thickness of the forced mixing layers. (a) Initial development of the layers (dashed black rectangle in c and d). (b) Difference between the $\overline{u}_N$-profiles at $x/\theta_i = 2.5$ of the forced and unforced mixing layers. (c) and (d) show growth of the mixing layers forced at $St_f = St_0 = 0.022$ and $St_f = St_0/2 = 0.011$. Dashed (blue) lines represent linear fits to different segments of the growth curves.

different forced mixing layers is presented in figure 7. The EFD forcing results in an initial development of the mixing layer occurring upstream compared to the unforced case. This is observed in the zoomed-in view of the vorticity thickness, close to the splitter-plate trailing edge (dashed black rectangle in figures 7c and d), shown in figure 7a. Regardless of the forced instability mode, the initial development of the forced mixing layer is at $x/\theta_i \approx 15$. This may be attributed to the action of the time-averaged momentum input by the DBD actuator against the splitter-plate wake.

In the work of Mehta[37], it is shown that the effect of the splitter-plate wake strength reduces with the velocity ratio r of the mixing layer. In the current scenario, the applied EFD forcing imparts momentum into the high-velocity boundary layer and accelerates the flow[20]. This will result in a local reduction of the velocity ratio just downstream of the splitter plate, which ultimately leads to the reduction of the strength of the splitter-plate wake.

An estimate of the local change of velocity ratio is made here. As reported in section II B, the maximum time-averaged velocity in the induced jet at the current operating conditions of $P_{avg,f} = 26.1$ W m^{-1} is estimated to be $U_f \approx 2.5$ m s^{-1}. This is comparable to the estimate of the induced velocity due to momentum input by the DBD actuator obtained from the PIV measurement. The difference of the $\overline{u}_N$ velocity profiles of the forced and unforced mixing layers ($\overline{u}_{N,St_f} - \overline{u}_{N,UML}$) at $x/\theta_i = 2.5$ is shown in figure 7b. The maximum difference in velocity due to forcing either instabilities is about 0.4, which in dimensional form is ($0.4 \cdot \Delta U$ =) 2 m s^{-1}. This estimate being lesser than that from the consumed power can be attributed to frictional losses incurred due to the presence of the splitter-plate surface downstream of the DBD actuator's plasma-generating edge. With this estimate from PIV (2 m s^{-1}), the velocity of the top stream close to the splitter-plate trailing edge can be approximated to be 12 m s^{-1}. Thus, just downstream of the trailing edge, the velocity ratio will be $r \approx 0.42$, instead of $r = 0.5$ in the unforced mixing layer, hence resulting in the weakening of the splitter-plate wake.

The initial growth of the forced mixing layer, indicating the roll-up of vortices, lasts until $x/\theta_i \approx 60$. Further downstream, forcing the two different instabilities results in different growth patterns of the ensuing mixing layers. Forcing the fundamental instability (figure 7c) reduces mixing layer growth significantly ($\approx 0.07 \cdot R$) until $x/\theta_i = 200$ compared to the unforced mixing layer. This is expected to be due to the attenuation of sub-harmonic instabilities[4] which play a pivotal role in mixing layer growth. The mixing layer then grows rapidly ($\approx 0.7 \cdot R$) until $x/\theta_i = 500$. Further downstream, the growth curve collapses on to that of the unforced mixing layer.

Application of forcing at the first sub-harmonic of the fundamental instability leads to a different growth curve (figure 7d). After the initial roll-up, the mixing layer starts to grow from $x/\theta_i \approx 100$, eventually attaining a linear growth at a rate of $\approx 0.43 \cdot R$, which is higher than the unforced mixing layer. Post this, the growth halts temporarily from $x/\theta_i \approx 300$ to about 600 ($\approx 0.089 \cdot R$). It is re-initiated further downstream and the layer grows linearly thereafter, until the end of the measured spatial domain, at a similar rate ($\approx 0.26 \cdot R$) as the unforced mixing layer. This growth curve bears qualitative similarity to those observed in the experimental efforts of Oster and Wygnanski[3], Ho and Huang[4] and Huang and Ho[11], when sub-harmonic forcing was applied on the mixing layer.

When the growth curves of the two forced mixing layers are compared with each other,

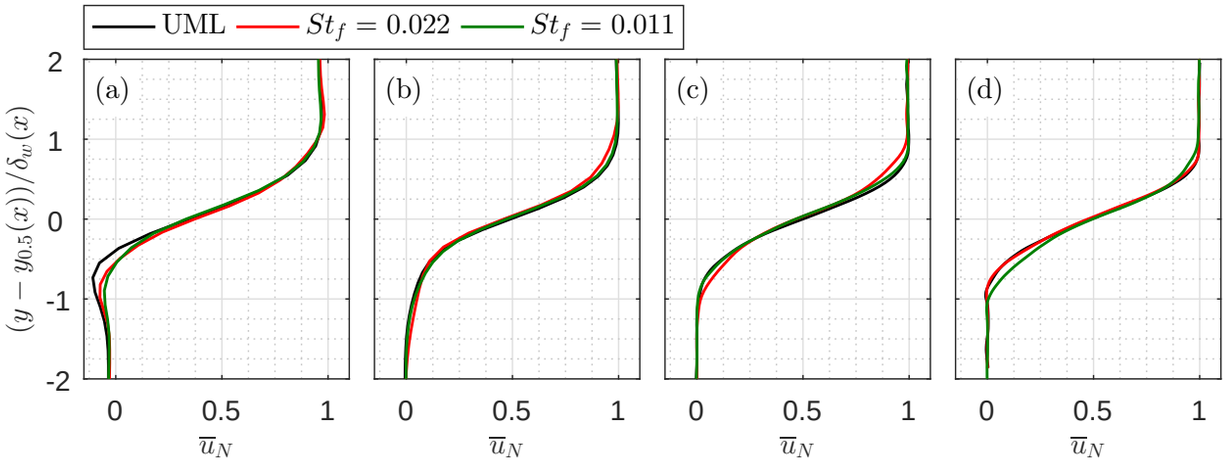

FIG. 8: Profiles of $\overline{u}_N$-velocity of the forced mixing layers at different streamwise locations; (a) $x/\theta_i = 60$, (b) $x/\theta_i = 130$, (c) $x/\theta_i = 400$, (d) $x/\theta_i = 600$.

one can observe that the streamwise location where the applied forcing has a significant influence varies. The effect of the fundamental KH instability forcing on the growth of the mixing layer is detected further upstream compared to when the sub-harmonic instability is forced. This is expected to be a consequence of the stability characteristics of the flow field, as perturbations pertaining to different instabilities are most amplified, and hence control the dynamics and growth of the layer, at different streamwise locations[4].

The $\overline{u}_N$-velocity profiles of the forced mixing layers at different streamwise stations are presented in figure 8. As in figure 5a, here too, the profiles are shifted with the $y_{0.5}$-location and non-dimensionalised with the vorticity thickness (δ_w(x)) at the corresponding streamwise station. Initially, the velocity defect in the forced mixing layers is lower compared to the unforced flow (see figure 8a) which once again indicates the reduction of the splitter-plate wake effect due to the applied forcing. At $x/\theta_i = 130$ (see figure 8b), where the unforced mixing layer attained self-similarity with respect to the mean flow quantities, the profiles of the forced mixing layers collapse on to that of the unforced flow. This implies that the applied forcing is not strong enough to modify the base-flow profile initially. Marginal differences in the profiles do develop further downstream, which are a result of the different growth curves of the corresponding forced mixing layers.

As done on the unforced mixing layer, the normalised power spectra of fluctuations of the transverse velocity component (v'), sampled along the $y_{o.5}$ line of the two forced mixing layers is presented in figure 9a and b. The amplitude of individual KH instabilities can be estimated

from the standard deviation of the corresponding fluctuations. This estimate is obtained here from the normalised power spectra along the $y_{0.5}$ line and is non-dimensionalised with $\overline{U}$ $((\Phi_N^{v'} \cdot \Delta f)^{1/2}/\overline{U})$. The variation of the amplitudes of the fundamental instability and its first sub-harmonic, along the streamwise direction, for the two forced mixing layers are shown in figure 9c and d.

The power spectra of the mixing layer forced at the fundamental KH instability (figure 9a) shows significant fluctuations at $St_f = St_0 = 0.022$. These appear just downstream of the splitter-plate trailing edge and span until about $x/\theta_i \approx 400$. This is further downstream compared to the unforced mixing layer, where fluctuations of the fundamental KH instability were very low after $x/\theta_i = 350$. Furthermore, the energy of fluctuations only at the forced instability is observed to be high here, unlike the unforced case where frequencies in a band around the fundamental instability were seen to contain high energy. The amplitude of the fundamental instability (see figure 9c) increases rapidly up to $x/\theta_i \approx 60$ at a rate of $\alpha_i \cdot \theta_i \approx 0.0037$, and decreases gradually thereafter, reaching an asymptotic level at $x/\theta_i = 600$. Strong fluctuations are also observed at the harmonic of the forced fundamental instability close to the splitter-plate trailing edge. Amplification of these harmonics are an artifact of the applied forcing. As demonstrated by Benard and Moreau[26], operating the DBD plasma actuator with a burst modulation results in strong fluctuations at the harmonics of the burst frequency within the induced flow, which in the current mixing layer, contributes to the strong spectral content at the harmonics of the forced fundamental instability. However, the energy in the frequency band of the sub-harmonic instabilities are significantly reduced compared to the unforced mixing layer, especially until $x/\theta_i \approx 200$. After the weakening of the fundamental instability, sub-harmonics in a broad-band spectrum amplify, which possibly drive mixing layer growth. This is also indicated in figure 9c, where the amplitude of the first sub-harmonic instability becomes higher than the fundamental instability at $x/\theta_i \approx 500$.

When the mixing layer is forced at $St_f = St_0/2 = 0.011$, fluctuations at the forced sub-harmonic instability are observed in the power spectra (figure 9b). These fluctuations are seen just downstream of the splitter-plate trailing edge. The amplitude of this instability along the streamwise direction is shown in figure 9d. The amplitude gradually increases, reaching its maximum value at $x/\theta_i \approx 300$, close to the location where the growth of this mixing layer came to a temporary halt. Beyond this location, the amplitude of this

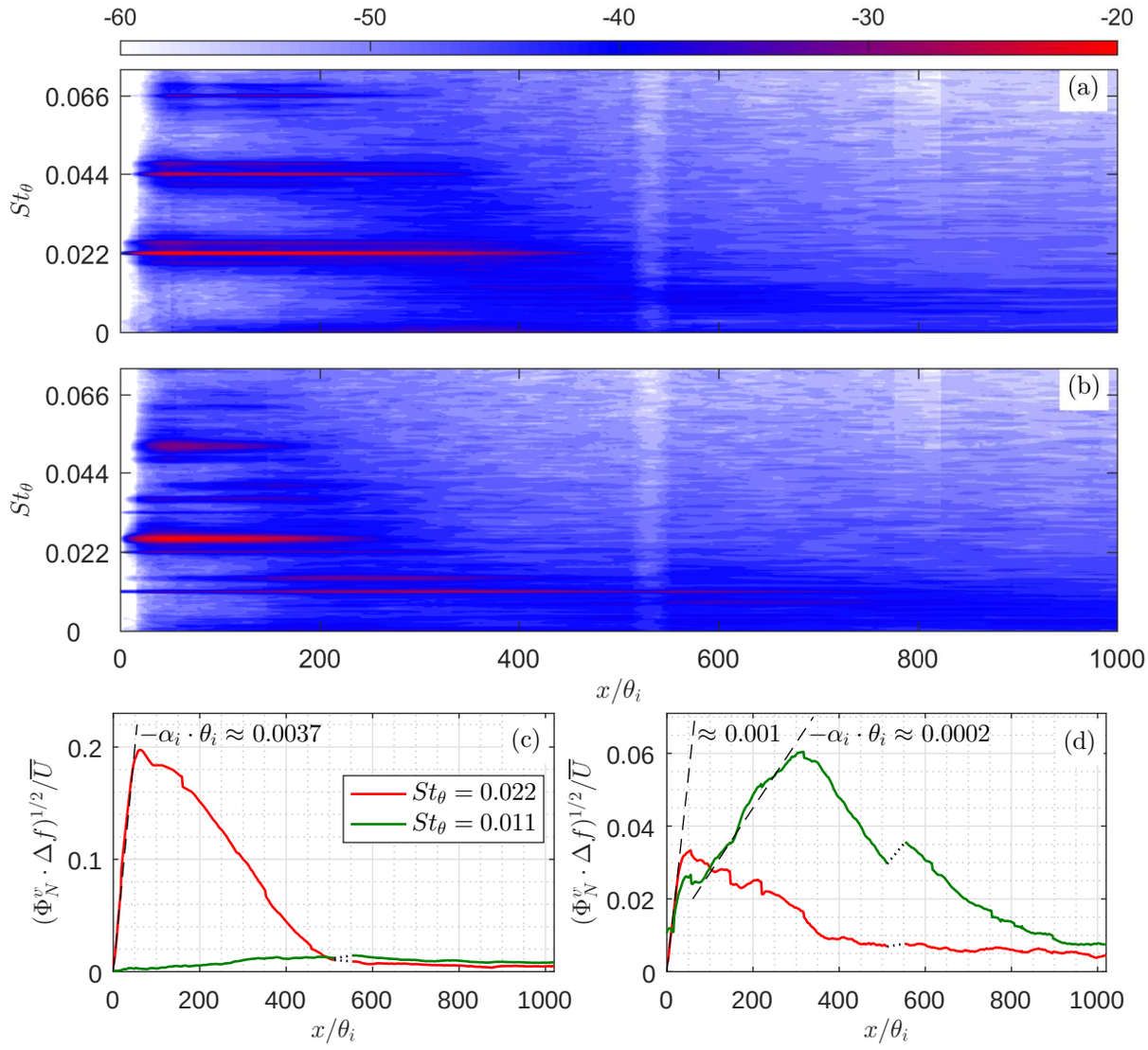

FIG. 9: Non-dimensional, normalised power spectra ($\Phi_N^{v'} \cdot \Delta f/\overline{U}^2$ (dB), $\Delta f = 5$ Hz) of the v'-velocity component sampled along the $y_{0.5}$ line of the mixing layers forced at (a) $St_f = St_0 = 0.022$ and (b) $St_f = St_0/2 = 0.011$. Non-dimensional amplitude of selected instabilities along the $y_{0.5}$ line for the two forced mixing layers are in (c) and (d). Estimate of the spatial amplification rate of these instabilities (dashed black lines) is also shown.

instability reduces and seems to reach an asymptotic level at the end of the measurement domain. Fluctuations at the fundamental instability (which is the harmonic of the forced instability) are also observed. The amplitude of this instability grows rapidly until $x/\theta_i \approx 50$ and reduces gradually thereafter. Additionally, until $x/\theta_i = 100$, the amplitude of this instability is higher than that of the forced sub-harmonic instability. Strong fluctuations are

observed around $St_\theta = 0.026$, starting just downstream of the splitter-plate trailing edge and lasting until $x/\theta_i \approx 200$ (see figure 9b). Finally, spectral content in the frequency band around $St_\theta = 0.15$ is also observed.

A comparison of the evolution of the amplitudes of the fundamental and the forced first sub-harmonic instability modes is now made. After the onset, these modes amplify at a similar rate ($\alpha_i \cdot \theta_i \approx 0.001$) until $x/\theta_i \approx 25$ indicating that these fluctuations are amplifying independently. The amplification rate of the sub-harmonic is reduced from $x/\theta_i \approx 44$, which signifies the onset of sub-harmonic resonance. Monkewitz[6], through their theoretical investigation established a critical fundamental instability amplitude of $\alpha_{crit}/\overline{U} = 0.0153 \cdot R^2$ was necessary for the occurrence of sub-harmonic resonance. This was confirmed experimentally by Thomas and Chu[9]. In the current mixing layer, the critical amplitude of the fundamental instability is significantly higher at $\alpha_{crit}/\overline{U} = 0.032$, and thus is sufficient to cause a phase-lock between the fundamental instability and the forced sub-harmonic as demonstrated by Husain and Hussain[8]. Consequently, as the amplitude of fluctuations corresponding to the fundamental instability begins to reduce, that of the forced first sub-harmonic instability increases. This is representative of the sub-harmonic being reinforced by energy transfer from the mean flow field that is oscillating at the fundamental instability. This leads to resonant growth of the sub-harmonic instability between $x/\theta_i \approx 80$ and 300, although at a modified rate of $\alpha_i \cdot \theta_i \approx 0.0002$.

Finally, another common feature linked to sub-harmonic resonance is the excitation of sub-harmonic sidebands[6,9,10]. These are a pair of modes with a frequency that is marginally deviated from the first sub-harmonic. When low-level broadband excitation is applied (as in the natural case), the resonant energy transfer not only excites the sub-harmonic but also excites locally most unstable modes. These competing modes cause an amplitude modulation of the sub-harmonic along the streamwise direction and also result in its suppression. Monkewitz[6] demonstrated that these sidebands are confined within the frequency band $St_0/2 \pm 0.08 \cdot St_0$, which is also corroborated by the experimental studies of Laufer and Zhang[10] and Thomas and Chu[9]. In the current mixing layer, apart from the forced first sub-harmonic itself, spectral content within the frequency band $St_f \pm 0.08 \cdot St_0 = 0.011 \pm 0.0018$ is very low (about 15 dB lower compared to the forced sub-harmonic, see figure 9b). The fluctuations centred around $St_\theta = 0.015$ is $0.18 \cdot St_0$ greater than the forced sub-harmonic. This difference is comparable to the width of the frequency band ($0.16 \cdot St_0$) where sideband

excitation can occur. While the fluctuations centred around $St_\theta = 0.015$ can be considered to be a sideband at $St_f + 2 \cdot 0.09 \cdot St_0$, a bias is apparent in this scenario as fluctuations at $St_f - 2 \cdot 0.09 \cdot St_0$ are very weak (about 15 dB lower than the forced sub-harmonic). Although, when the streamwise evolution of the sub-harmonic is considered (see figure 9d), no amplitude-modulation or suppression of the corresponding fluctuations is observed. Thus, the applied forcing here seems to not excite sub-harmonic sidebands. This indicates that the applied EFD forcing is not of a broadband nature but is rather locked to the selected burst frequency and its harmonics.

The results discussed until now demonstrate that forcing different KH instabilities has specific effects on the growth of the mixing layer owing to the alteration of the spectral content within. The effect of the applied EFD forcing on the dynamics and interactions of coherent vortices is now desired. The PIV acquisition was synchronized with the burst-modulation cycle. Thus, the phase-average of the instantaneous PIV time-series was computed at eight different phases separated by 0.25π of the burst modulation. The vorticity (ω_z) and Q-criterion (second invariant of the velocity vector field[40]), are computed and utilized to detect the coherent vortex cores in the mixing layer, and observe their dynamics and interaction. These results, for the two forced mixing layers, are presented in figures 10 and 11. The vorticity is non-dimensionalised with $\theta_i/\overline{U}$ and the Q-criterion is non-dimensionalised with the maximum value (Q_{max}) in the corresponding field.

The application of EFD forcing to excite the fundamental KH instability results in amplification of the corresponding two-dimensional primary KH instability wave which rolls-up into coherent vortices just downstream of the splitter-plate trailing edge, as observed in the phase-averaged fields in figure 10. The roll-up occurs during the amplification of this instability, observed in figure 9c and is expected to be completed at $x/\theta_i \approx 60$, when the amplitude of this instability reaches its maximum value. This also corroborates well with the growth curve of this mixing layer presented in figure 7c. Additionally, the convection velocity of these coherent vortices is equal to the expected value of $\overline{U} = 7.5$ m s^{-1} (see ref. 21) after the initial roll-up of vortices is complete.

However, no instance of vortex pairing is observed along the burst-modulation cycle. Low energy of sub-harmonic instabilities compared to the fundamental instability observed in the power spectra (see figure 9a and c) seems to inhibit the vortex pairing process as was also shown in previous research efforts[3,4,8]. This inhibition of vortex interaction results in

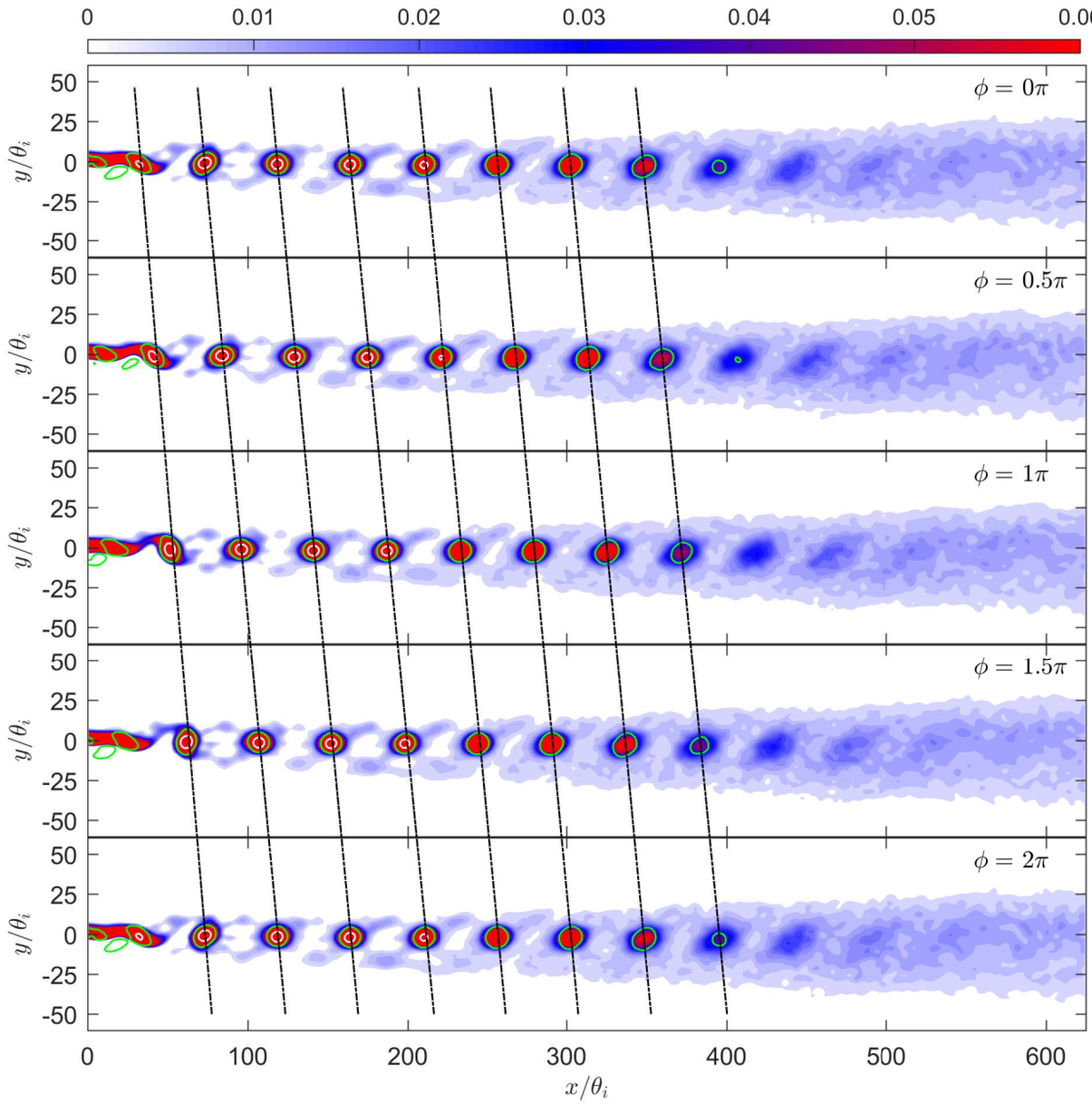

FIG. 10: Phase-averaged fields of the mixing layer forced at $St_f = St_0 = 0.022$ ($f_b = 300$ Hz) at five different phases along the burst modulation. Colour scale: non-dimensional vorticity ($-\omega_z \cdot \theta_i/\overline{U}$). Contour lines: non-dimensional Q-criterion (Q/Q_{max}, green: $0.02 \cdot Q_{max}$; white: $0.5 \cdot Q_{max}$).

the negligible growth of this mixing layer until $x/\theta_i = 200$ seen in figure 7c. These effects are not expected to be a consequence of the initial amplitude of the applied forcing, but rather the manner in which the perturbation is introduced. Imparting fluctuations into the

high-velocity side splitter-plate boundary layer seems to condition the flow field downstream more effectively, leading to inhibition of vortex pairing and the linear growth regime being bypassed. The strength of the coherent vortices seem to diminish along the streamwise direction, especially downstream of $x/\theta_i \approx 300$ and there are no clear vortices noticeable after $x/\theta_i \approx 450$. Thus, the current forced mixing layer is not in phase with the burst frequency of the applied EFD forcing any more. This, along with the observations made in figure 9a and c, further support the idea that the re-initiation of growth downstream of $x/\theta_i = 200$ must be a consequence of the natural amplification of sub-harmonic instabilities.

The phase-averaged fields of the mixing layer when the first sub-harmonic of the fundamental KH instability is forced are shown in figure 11. One instance of vortex pairing involving two vortices (dashed red rectangle in the field at phase $\phi = 0$) is observed in this forced mixing layer. The amalgamation process of these vortices along the burst-modulation cycle is depicted in the snapshots presented in figure 12. The non-linear interaction of the forced sub-harmonic instability with the naturally present fundamental KH instability seems to result in the roll-up of vortices alternately close to and farther from their neighbours. The two vortices that are close to each other are observed to undergo pairing due to mutual induction. The vortex pairing process begins at $x/\theta_i \approx 100$, which corresponds to the location where the amplitude of the forced sub-harmonic KH instability becomes more than that of the fundamental instability as observed in figure 9d. The pairing process ends close to where the amplitude of the forced instability reaches its maximum value, at about $x/\theta_i \approx 280$. The pairing process is completed within two burst-modulation cycles, thus resulting in the higher growth rate seen in figure 7d for this mixing layer.

The wavelength of fluctuations in the frequency band around $St_\theta = 0.015$ (which was observed to be amplified in figure 9b) computed by $\lambda_\theta/\theta_i = 1/St_\theta$ $(= \overline{U}/f_b\theta_i)$ ranges between 62 and 74. Interestingly, the distance between the weaker vortex in the merging pair and the stronger vortex downstream (not the pairing vortex-pair) is in that range. Thus, the fluctuations in this frequency band are in fact an artefact of the vortex passage frequency induced by the pairing process, rather than an instability. The fluctuations in the frequency band around $St_\theta = 0.026$ is due to the pairing process as well. This is a result of the passage of the pairing vortices which are displaced such that they are closer to one another from the onset of the mixing layer. It is worth noting that this frequency is the sum of the frequency of the forced instability $St_f = 0.011$ and that of the fluctuations around $St_\theta = 0.015$,

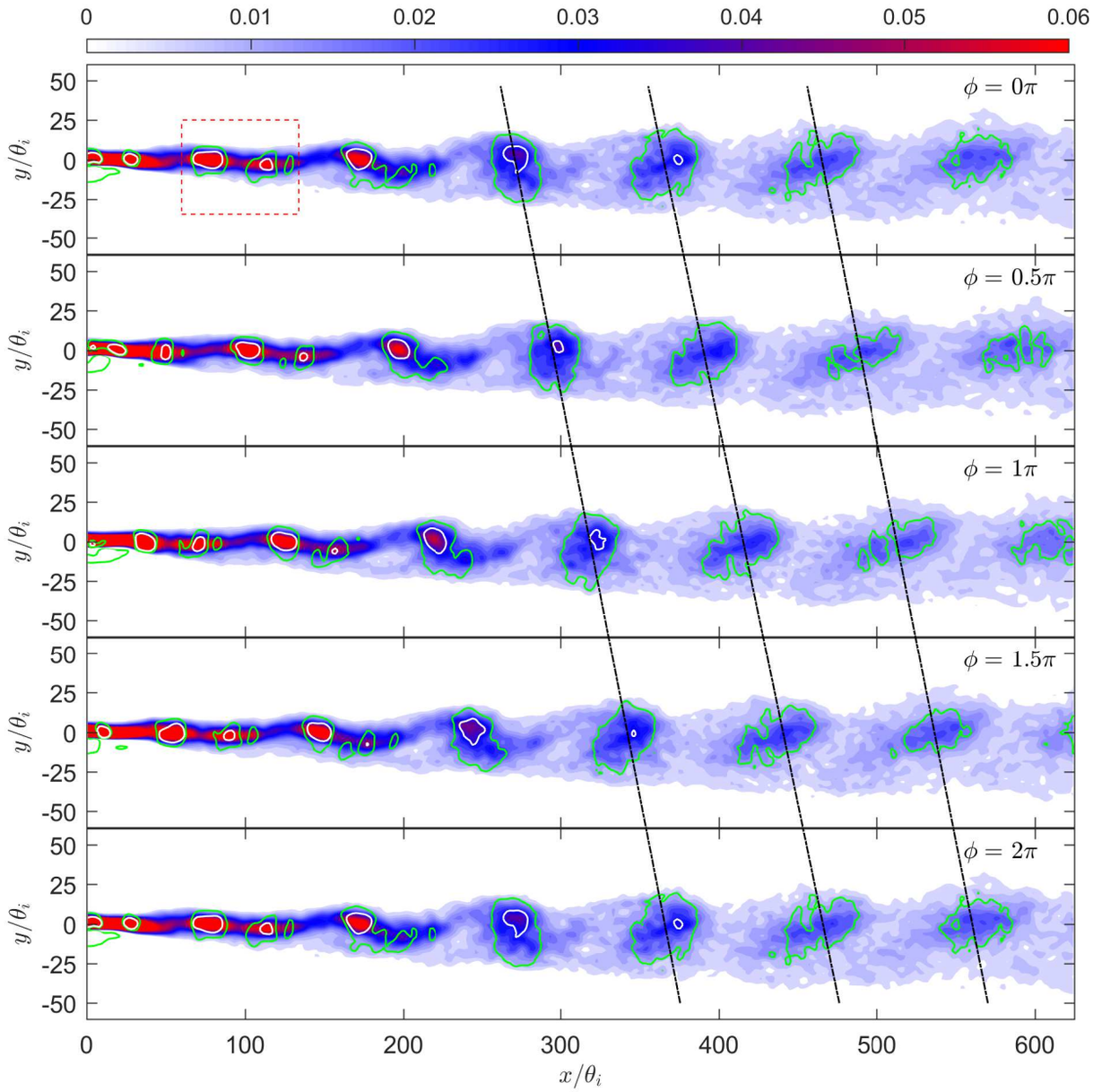

FIG. 11: Phase-averaged fields of the mixing layer forced at $St_f = St_0 = 0.011$ ($f_b = 150$ Hz) at five different phases along the burst modulation. Colour scale: non-dimensional vorticity ($-\omega_z \cdot \theta_i/\overline{U}$). Contour lines: non-dimensional Q-criterion (Q/Q_{max}, green: $0.02 \cdot Q_{max}$; white: $0.2 \cdot Q_{max}$).

suggesting a favourable phase relation between these modes.

The coherent vortices show no interaction after the completion of the vortex pairing as seen with the case of fundamental instability forcing, which explains the temporary halt in

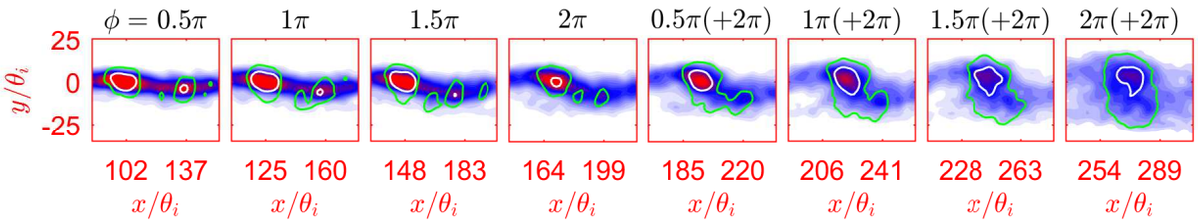

FIG. 12: Snapshots of vortex pairing in the mixing layer forced at $St_f = St_0 = 0.011$ (dashed red rectangle at phase $\phi = 0$ in figure 11) along the burst-modulation cycle. Colour scale: non-dimensional vorticity ($-\omega_z \cdot \theta_i/\overline{U}$). Contour lines: non-dimensional Q-criterion (Q/Q_{max}, green: $0.02 \cdot Q_{max}$; white: $0.2 \cdot Q_{max}$).

the growth. This is expected to be due to the amplitude of forcing being strong enough to cause resonance of the imparted fluctuations[3,8]. In fact, this region is bounded within $1 < RSt_f x/\theta_i < 2$, as proposed by Oster and Wygnanski[3] based on their observations. The resonance renders the forced sub-harmonic instability to have a higher amplitude, especially in comparison with the fundamental instability (as observed in figures 9b and d), and leads to a train of vortices that do not interact with each other. Thus, it may be inferred here that, not just the presence of sub-harmonic instabilities, but their relative energy level with respect to the fundamental instability governs the vortex pairing process.

After the pairing, the vortices convect downstream at a velocity of about 8 m s^{-1} which is comparable to the expected value. Here too, the vortices become weaker and eventually disappear after $x/\theta_i \approx 600$ (not shown here). The linear growth of the mixing layer after this streamwise station is mainly attributed to the natural onset of other instabilities with frequencies lower than the forced sub-harmonic instability.

V. CONCLUDING REMARKS

The influence of EFD forcing applied by a DBD plasma actuator on the coherent vortices in a two-dimensional plane mixing layer generated due to the interaction of two air streams at different velocities is investigated experimentally in this work. The effect of imparting fluctuations pertaining to the fundamental KH instability and its first sub-harmonic on the growth of the mixing layer and the interaction of the vortices within, is studied here. It is observed that exciting these instabilities by introducing perturbations into the boundary

layer on the high-velocity side of the splitter plate is effective in conditioning the mixing layer flow configuration that ensues downstream.

The results demonstrate that the applied EFD forcing, specifically the burst frequency, has a significant effect on the generation of spanwise vortices, their subsequent pairing and as a consequence, the growth of the mixing layer. Amplification of the fundamental KH instability results in the inhibition of vortex pairing and consequently a local negligible growth of the ensuing mixing layer. This is due to the attenuation of sub-harmonic instabilities, which reiterates their necessity for the occurrence of vortex pairing[4,7,8]. Imparting fluctuations at the first sub-harmonic of the fundamental instability, as expected, results in one instance of vortex pairing involving two vortices. The growth rate of the mixing layer is observed to be higher than the unforced case in the streamwise region where the vortex pairing process takes place. The growth stagnates thereafter owing to sub-harmonic resonance, which results in a train of vortices that show no interaction. In both forced cases, the mixing layer eventually acquires a growth rate similar to that of the unforced mixing layer. Additionally, forcing different KH instabilities is seen to affect the mixing layer at different streamwise locations. This is indicative of the applied forcing manipulating the stability characteristics of the flow field, ultimately resulting in the observed dynamics.

As a next step, using composite signals that manipulate both the fundamental and sub-harmonic instabilities simultaneously should be attempted. This exercise will not only help govern the relative energy levels of these instabilities, but also open the possibility to analyse the effect of the phase difference between the two waves. Further research is also necessary to investigate the influence of the operating parameters of the DBD actuator on the mixing layer, in order to design more efficient control strategies in the future. Finally, the effectiveness of the applied forcing in manipulating the shear layer, combined with the fast response of a DBD plasma actuator to exercise the necessary control, makes it an ideal candidate to be included in closed-loop control algorithms, which should also be attempted in the future.

ACKNOWLEDGMENTS

This research is funded by the French Government program *Investissements d'Avenir* (LABEX INTERACTIFS, reference ANR-11-LABX-0017-01).

DATA AVAILABILITY

The data that support the findings of this study are available from the corresponding author upon reasonable request.

REFERENCES

[1]G. Brown and A. Roshko, "On density effects and large structure in turbulent mixing layers," Journal of Fluid Mechanics **64**, 775–816 (1974).

[2]C. Winant and F. Browand, "Vortex pairing: the mechanism of turbulent mixing-layer growth at moderate reynolds number," Journal of Fluid Mechanics **63**, 237–255 (1974).

[3]D. Oster and I. Wygnanski, "The forced mixing layer between parallel streams," Journal of Fluid Mechanics **123**, 91–130 (1982).

[4]C. Ho and L. Huang, "Subharmonics and vortex merging in mixing layers," Journal of Fluid Mechanics **119**, 443–473 (1982).

[5]R. Kelly, "On the stability of an inviscid shear layer which is periodic in space and time," Journal of Fluid Mechanics **27**, 657–689 (1967).

[6]P. Monkewitz, "Subharmonic resonance, pairing and shredding in the mixing layer," Journal of Fluid Mechanics **188**, 223–252 (1988).

[7]N. Mansour, F. Hussain, and J. Buell, "Subharmonic resonance in a mixing layer," Center for Turbulence Research , 57–68 (1988).

[8]H. Husain and F. Hussain, "Experiments on subharmonic resonance in a shear layer," Journal of Fluid Mechanics **304**, 343–372 (1995).

[9]F. Thomas and H. Chu, "An experimental investigation of the transition of a planar jet: Subharmonic suppression and upstream feedback," Physics of Fluids **1**, 1566–1587 (1989).

[10]J. Laufer and J. Zhang, "Unsteady aspects of a low mach number jet," Physics of Fluids **26**, 1740–1750 (1983).

[11]L. Huang and C. Ho, "Small-scale transition in a plane mixing layer," Journal of Fluid Mechanics **210**, 475–500 (1990).

[12]R. Mathis, E. Collin, J. Delville, and J. Bonnet, "Analysis of a plane turbulent mixing layer manipulated by a localized forced separation," Journal of Turbulence , N56 (2007).

[13]V. Parezanović, J. Laurentie, C. Fourment, J. Delville, J. Bonnet, A. Spohn, T. Duriez, L. Cordier, B. Noack, M. Abel, M. Segond, T. Shaqarin, and B. S.L., "Mixing layer manipulation experiment," Flow, turbulence and combustion **94**, 155–173 (2014).

[14]A. Glezer and M. Amitay, "Synthetic jets," Annual review of fluid mechanics **34**, 503–529 (2002).

[15]N. Benard and E. Moreau, "Electrical and mechanical characteristics of surface ac dielectric barrier discharge plasma actuators applied to airflow control," Experiments in Fluids **55**, 1–43 (2014).

[16]S. Grundmann and C. Tropea, "Active cancellation of artificially introduced tollmien–schlichting waves using plasma actuators," Experiments in Fluids **44**, 795–806 (2008).

[17]S. Yadala, M. Hehner, J. Serpieri, N. Benard, P. Dörr, M. Kloker, and M. Kotsonis, "Experimental control of swept-wing transition through base-flow modification by plasma actuators," Journal of Fluid Mechanics **844** (2018).

[18]T. Corke and F. Thomas, "Active and passive turbulent boundary-layer drag reduction," AIAA Journal , 1–13 (2018).

[19]R. Ely and J. Little, "The mixing layer perturbed by a dielectric barrier discharge," in *43rd AIAA Fluid Dynamics Conference* (2013) p. 2753.

[20]A. Singh and J. Little, "A comparative study of ac-dielectric barrier discharge versus ns-dielectric barrier discharge plasma actuators in an incompressible turbulent mixing layer," Journal of Physics D: Applied Physics **53**, 164004 (2020).

[21]D. Oster, I. Wygnanski, and H. Fiedler, "Some preliminary observations on the effect of initial conditions on the structure of the two-dimensional turbulent mixing layer," Turbulence in Internal Flows (ed. S.N.B. Murthy) , 67–87 (1977).

[22]J. Pons, E. Moreau, and G. Touchard, "Asymmetric surface dielectric barrier discharge in air at atmospheric pressure: electrical properties and induced airflow characteristics," J. Phys. D: Appl. Phys. **38**, 3635 (2005).

[23]M. Forte, J. Jolibois, J. Pons, E. Moreau, G. Touchard, and M. Cazalens, "Optimization of a dielectric barrier discharge actuator by stationary and non-stationary measurements of the induced flow velocity: application to airflow control," Exp. Fluids **43**, 197–928 (2007).

[24]A. Debien, N. Benard, and E. Moreau, "Streamer inhibition for improving force and electric wind produced by dbd actuators," J. Phys. D: Appl. Phys. **45**, 215201 (2012).

[25]N. Benard and E. Moreau, "Electric wind produced by a surface plasma discharge energized by a burst modulated high voltage," in *Proceedings of the 29th International Conference on Plasma Ionized Gazss (ICPIG)* (2009) pp. 12–17.

[26]N. Benard and E. Moreau, "Capabilities of the dielectric barrier discharge plasma actuator for multi-frequency excitations," J. Phys. D: Appl. Phys. **43**, 145201 (2010).

[27]J. Jolibois and E. Moreau, "Enhancement of the electromechanical performances of a single dielectric barrier discharge actuator," IEEE Transactions on Dielectrics and Electrical Insulation **16**, 758–767 (2009).

[28]M. Raffel, C. Willert, S. Wereley, and J. Kompenhans, *Particle image velocimetry* (2007).

[29]A. Sciacchitano and B. Wieneke, "Piv uncertainty propagation," Measurement Science and Technology **27**, 084006 (2016).

[30]S. Laizet, S. Lardeau, and E. Lamballais, "Direct numerical simulation of a mixing layer downstream a thick splitter plate," Physics of Fluids **22**, 015104 (2010).

[31]A. Michalke, "On spatially growing disturbances in an inviscid shear layer," Journal of Fluid Mechanics **23**, 521–544 (1965).

[32]G. Abramovich, *The theory of turbulent jets* (MIT Press, 1963).

[33]C. Sabin, "An analytical and experimental study of the plane, incompressible, turbulent free-shear layer with arbitrary velocity ratio and pressure gradient," Journal of Basic Engineering **87**, 421–428 (1965).

[34]N. Pui and I. Gartshore, "Measurements of the growth rate and structure in plane turbulent mixing layers," Journal of Fluid Mechanics **91**, 111–130 (1979).

[35]A. Townsend, *The structure of turbulent shear flow* (Cambridge University Press, 1976).

[36]J. Bell and R. Mehta, "Development of a two-stream mixing layer from tripped and untripped boundary layers," AIAA journal **28**, 2034–2042 (1990).

[37]R. Mehta, "Effect of velocity ratio on plane mixing layer development: Influence of the splitter plate wake," Experiments in Fluids **10**, 194–204 (1991).

[38]C. Braud, D. Heitz, G. Arroyo, L. Perret, J. Delville, and J. Bonnet, "Low-dimensional analysis, using pod, for two mixing layer–wake interactions," International Journal of Heat and Fluid Flow **25**, 351–363 (2004).

[39]C. Ho and P. Huerre, "Perturbed free shear layers," Annual Review of Fluid Mechanics **16**, 365–422 (1984).

[40]J. Hunt, A. Wray, and P. Moin, "Eddies, streams, and convergence zones in turbulent flows," Center for Turbulence Research Report CTR-S88 , 193208 (1988).

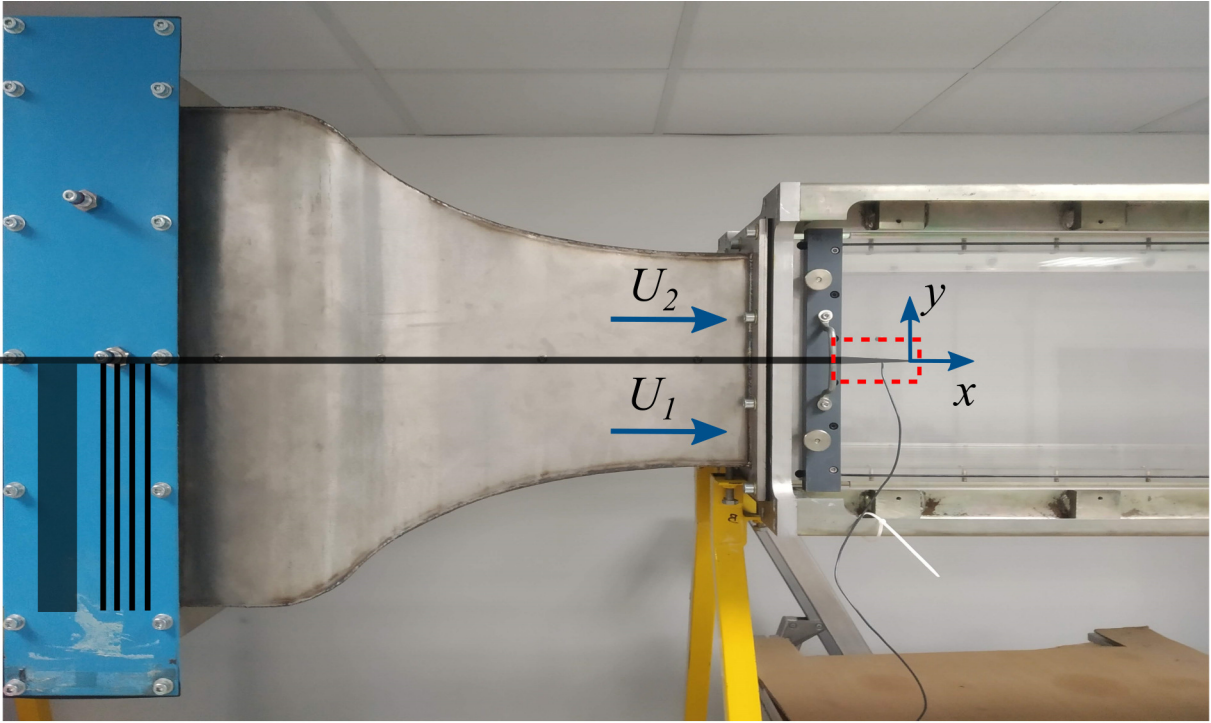
U_2
U_1
y
x

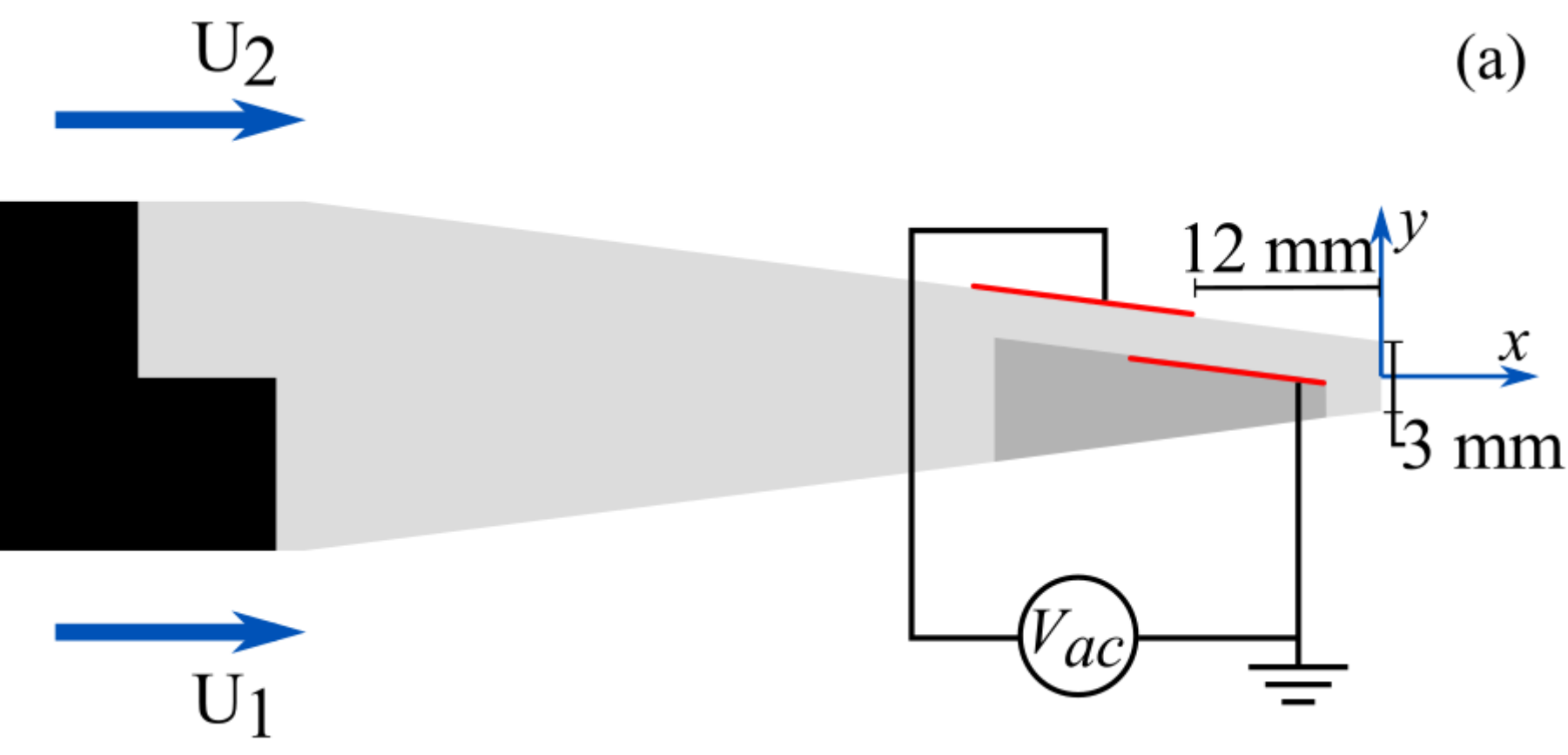
U2
(a)
12 mm
y
x
3 mm
Vac
U1

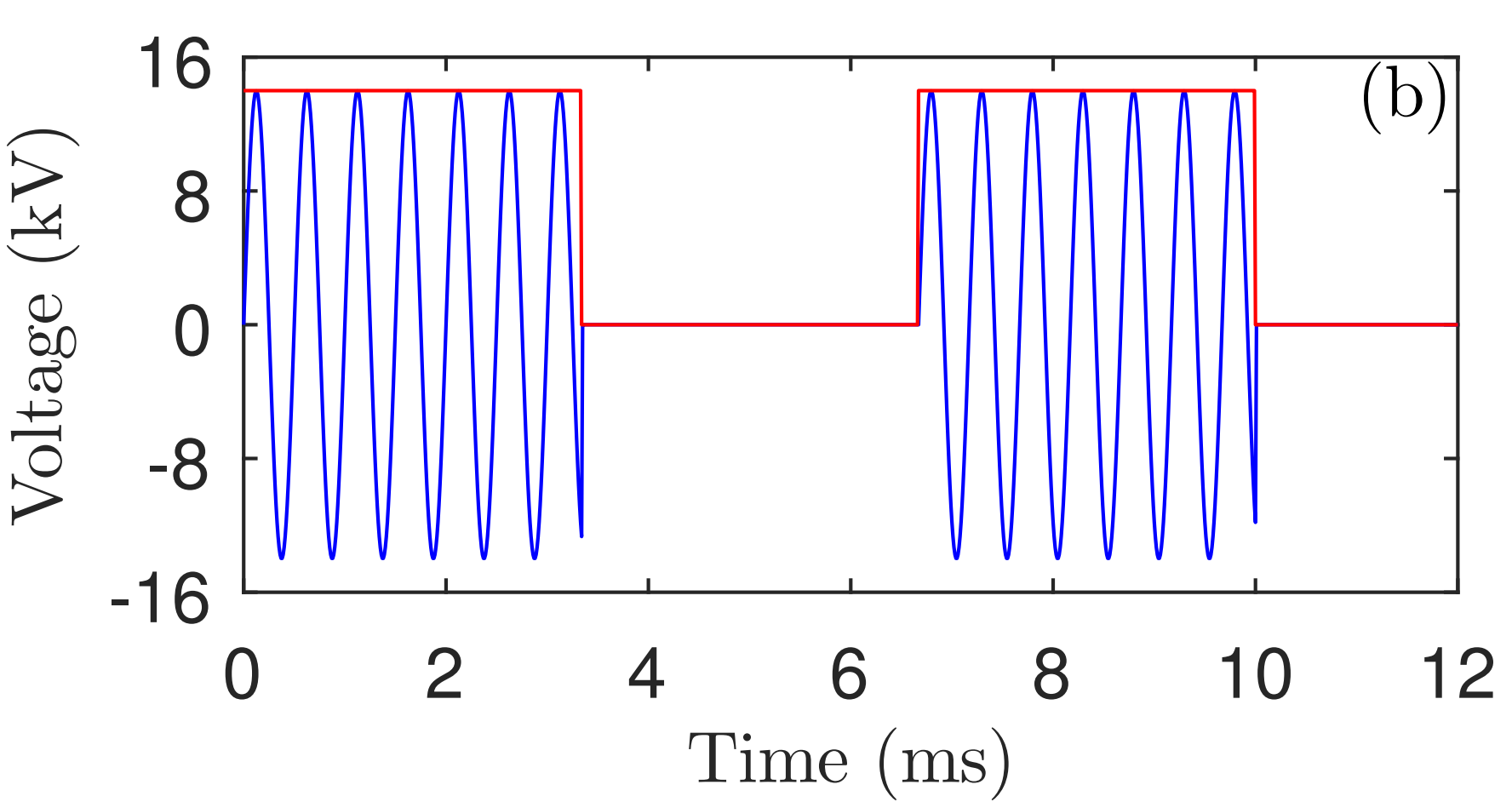
(b)
16
8
0
-8
-16
Voltage (kV)
0
2
4
6
8
10
12
Time (ms)

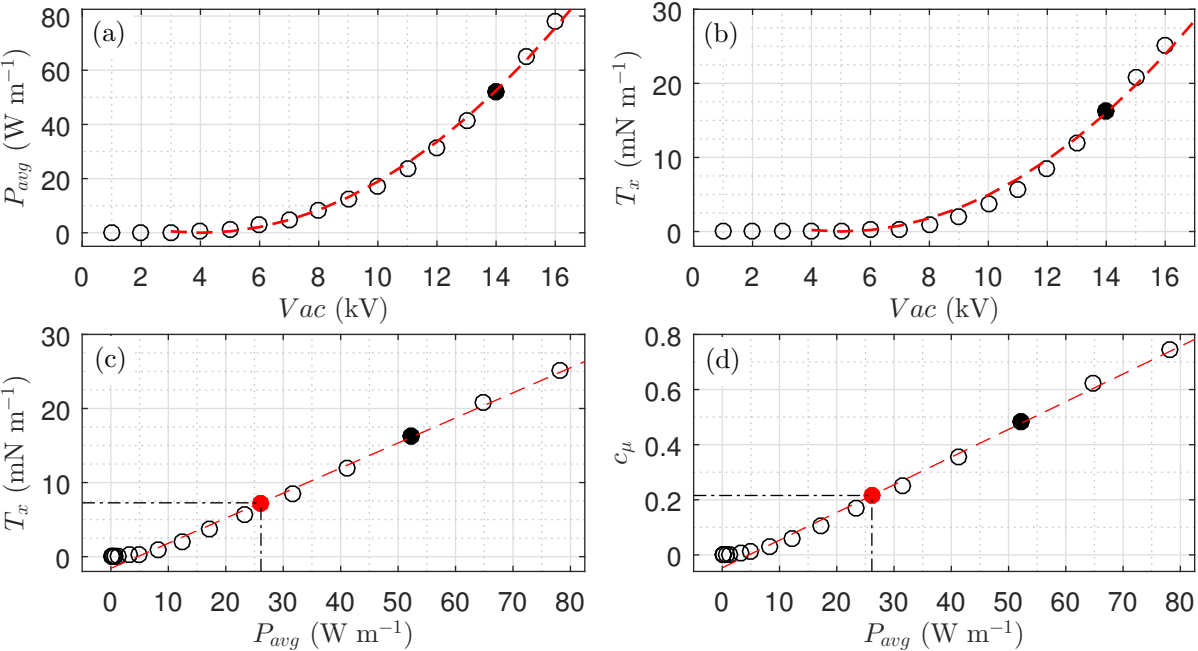
(a)
P_{avg} (W m^{-1})
Vac (kV)
(b)
T_x (mN m^{-1})
Vac (kV)
(c)
T_x (mN m^{-1})
P_{avg} (W m^{-1})
(d)
c_μ
P_{avg} (W m^{-1})

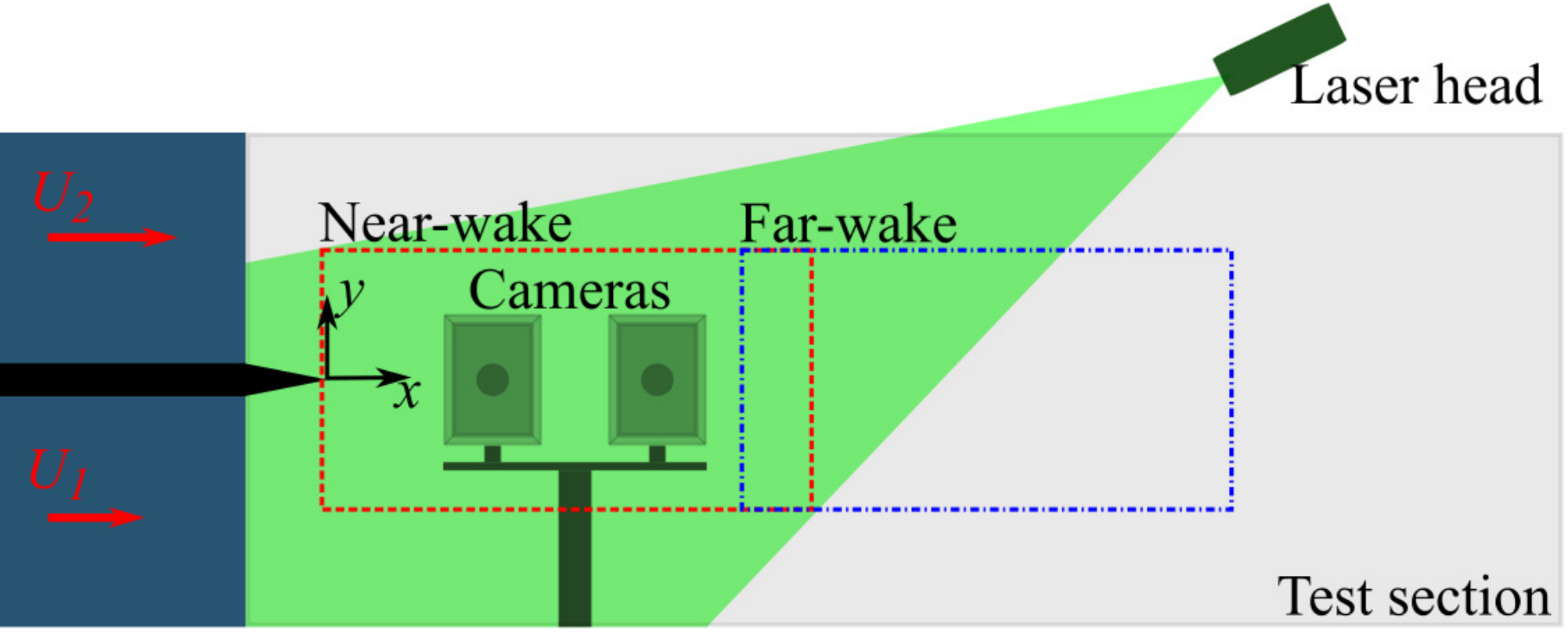
Laser head
U_2
Near-wake
Far-wake
y
Cameras
x
U_1
Test section

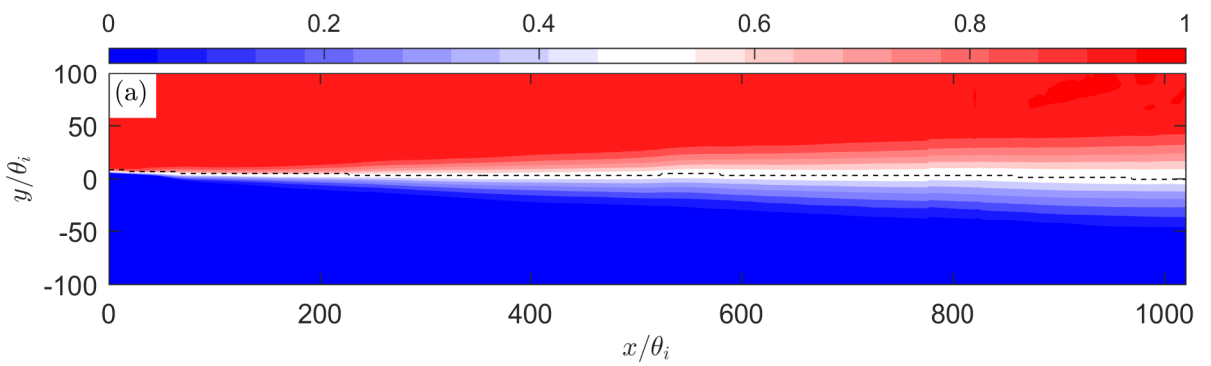
0
0.2
0.4
0.6
0.8
1
(a)
100
50
0
-50
-100
y/θ_i
0
200
400
600
800
1000
x/θ_i

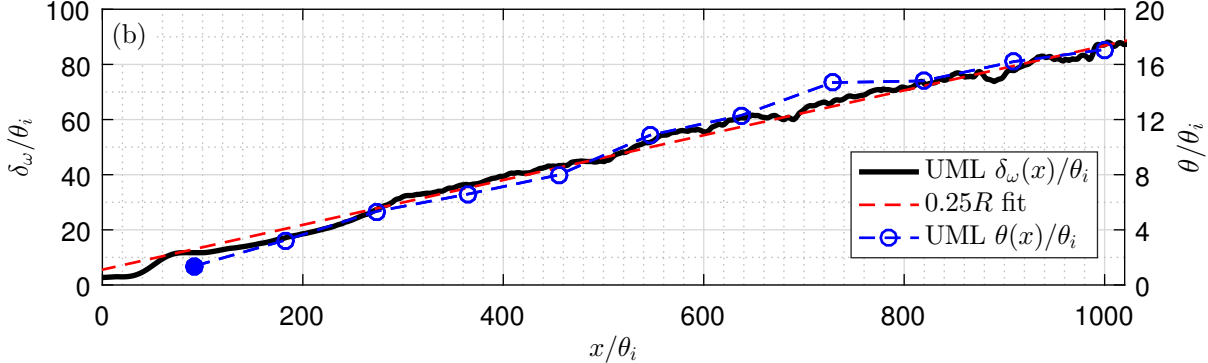
(b)
δ_ω/θ_i
θ/θ_i
x/θ_i
UML $\delta_\omega(x)/\theta_i$
$0.25R$ fit
UML $\theta(x)/\theta_i$
0
20
40
60
80
100
200
400
600
800
1000
4
8
12
16

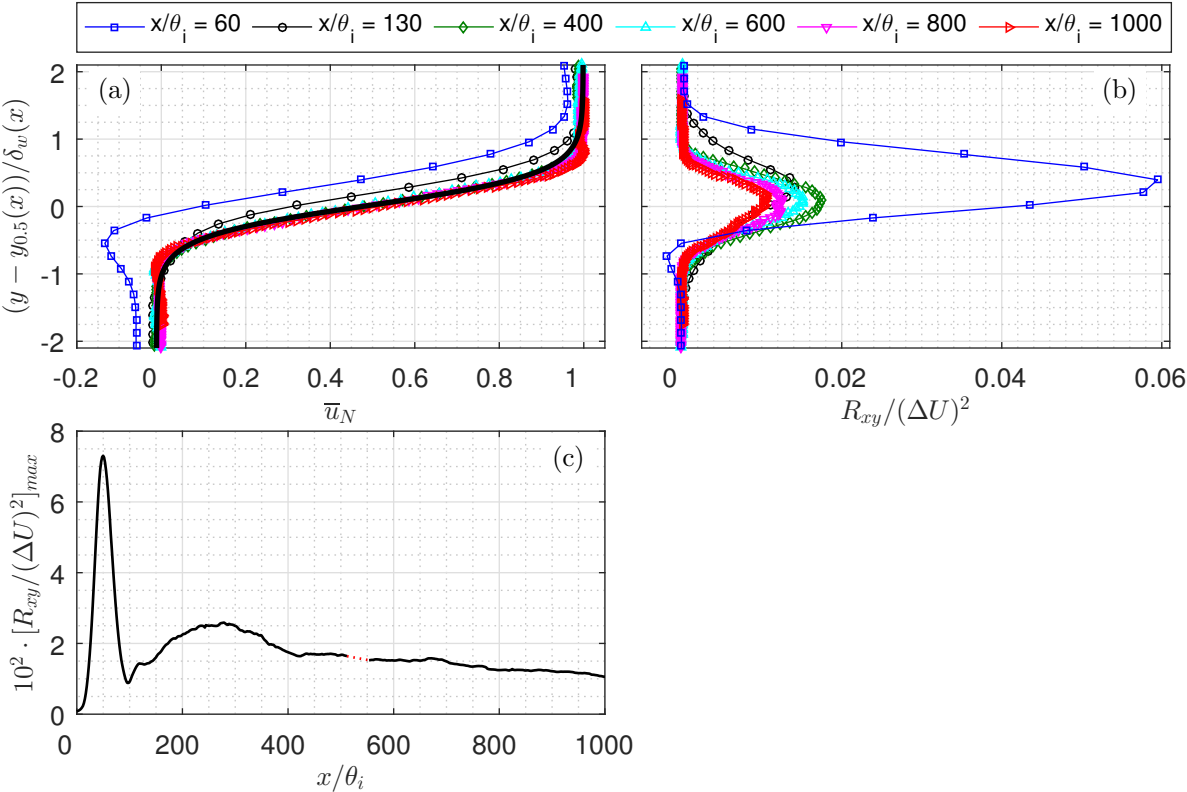
x/θi = 60
x/θi = 130
x/θi = 400
x/θi = 600
x/θi = 800
x/θi = 1000
(a)
(b)
(c)
$(y - y_{0.5}(x))/\delta_w(x)$
$\overline{u}_N$
$R_{xy}/(\Delta U)^2$
$10^2 \cdot [R_{xy}/(\Delta U)^2]_{max}$
x/θ_i

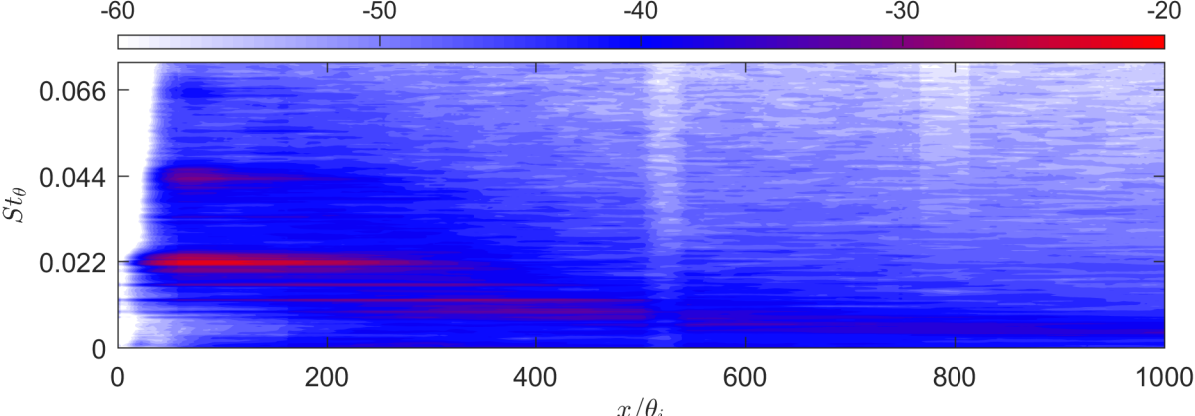
-60
-50
-40
-30
-20
0.066
0.044
0.022
0
St_θ
0
200
400
600
800
1000
x/θ_i

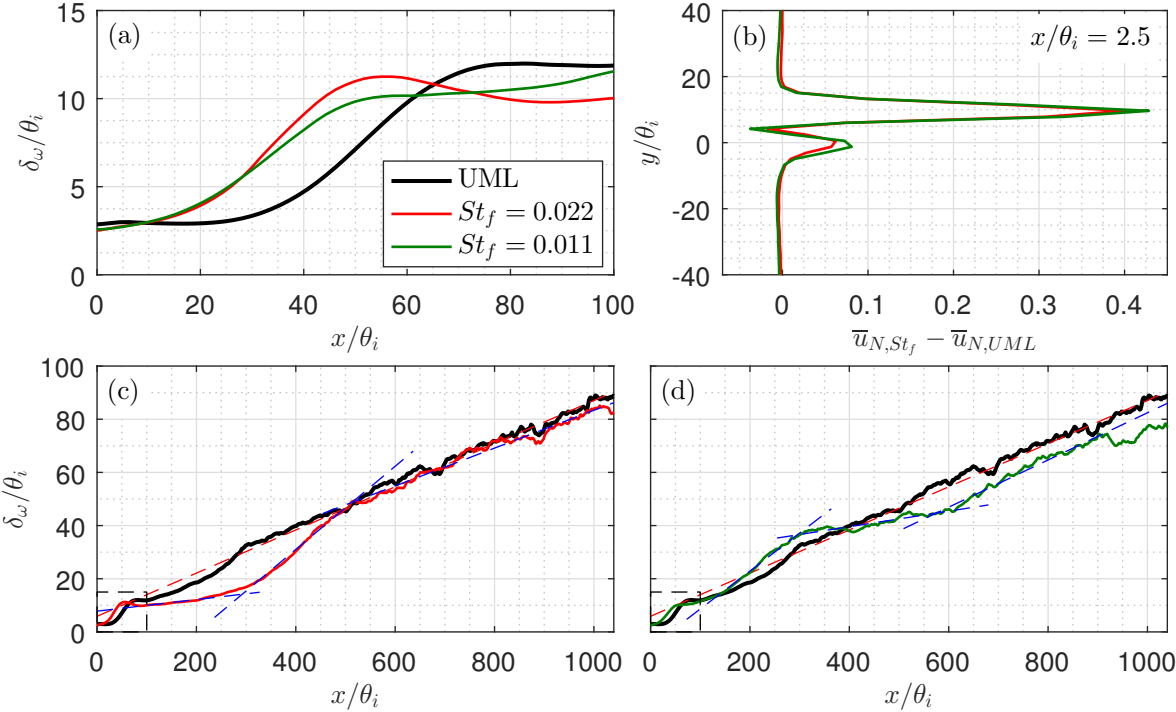
(a)
δ_ω/θ_i
x/θ_i
UML
$St_f = 0.022$
$St_f = 0.011$
(b)
$x/\theta_i = 2.5$
y/θ_i
$\overline{u}_{N,St_f} - \overline{u}_{N,UML}$
(c)
δ_ω/θ_i
x/θ_i
(d)
x/θ_i

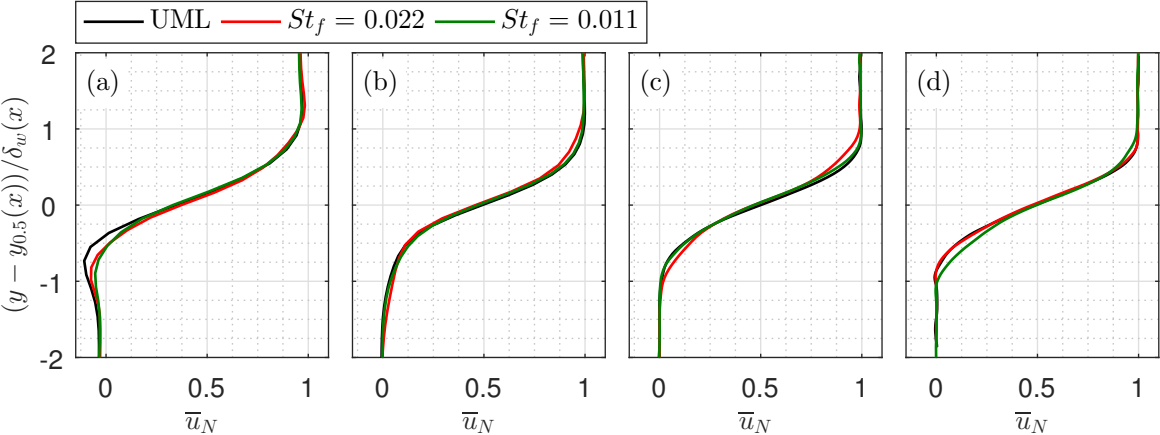
UML
$St_f = 0.022$
$St_f = 0.011$
(a)
(b)
(c)
(d)
$(y - y_{0.5}(x))/\delta_w(x)$
2
1
0
-1
-2
0
0.5
1
$\overline{u}_N$

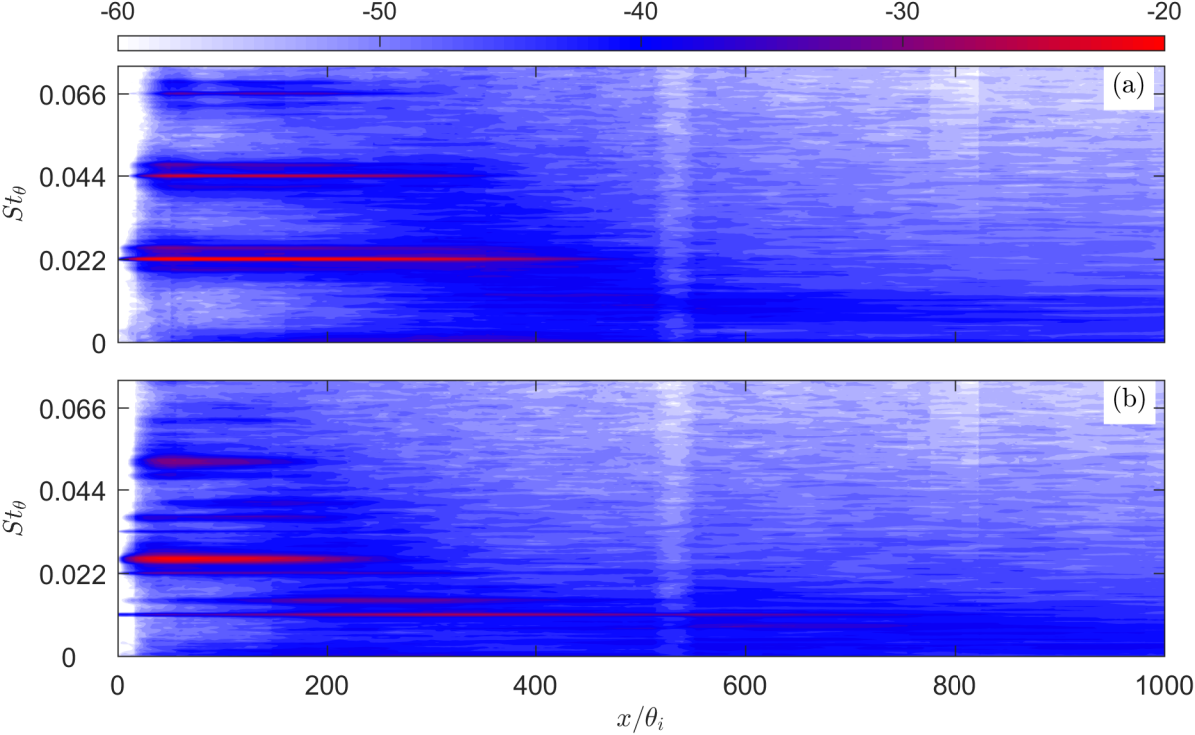
-60
-50
-40
-30
-20
(a)
(b)
St_θ
0.066
0.044
0.022
0
0
200
400
600
800
1000
x/θ_i

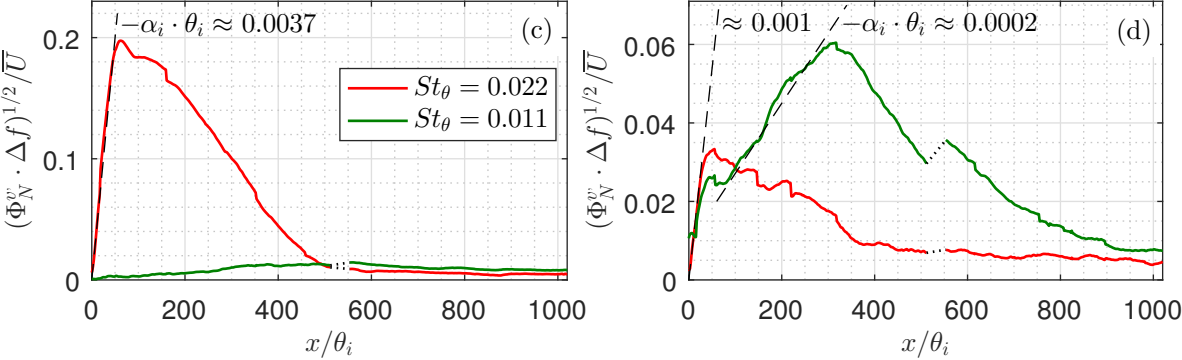
$-\alpha_i \cdot \theta_i \approx 0.0037$
(c)
$St_\theta = 0.022$
$St_\theta = 0.011$
$(\Phi_N'' \cdot \Delta f)^{1/2}/\overline{U}$
x/θ_i
≈ 0.001
$-\alpha_i \cdot \theta_i \approx 0.0002$
(d)
$(\Phi_N'' \cdot \Delta f)^{1/2}/\overline{U}$
x/θ_i

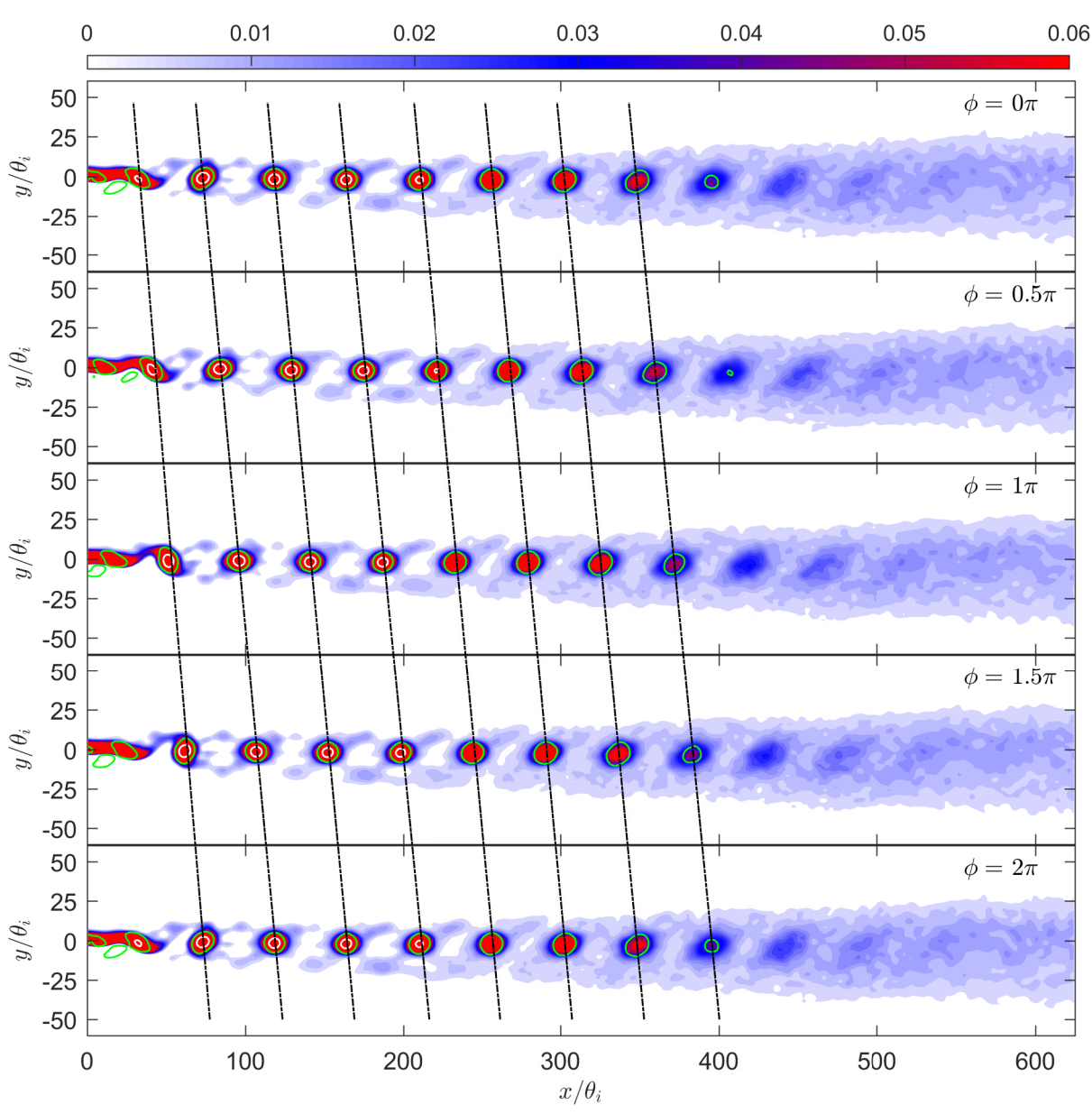
0
0.01
0.02
0.03
0.04
0.05
0.06
$\phi = 0\pi$
$\phi = 0.5\pi$
$\phi = 1\pi$
$\phi = 1.5\pi$
$\phi = 2\pi$
y/θ_i
50
25
0
-25
-50
0
100
200
300
400
500
600
x/θ_i

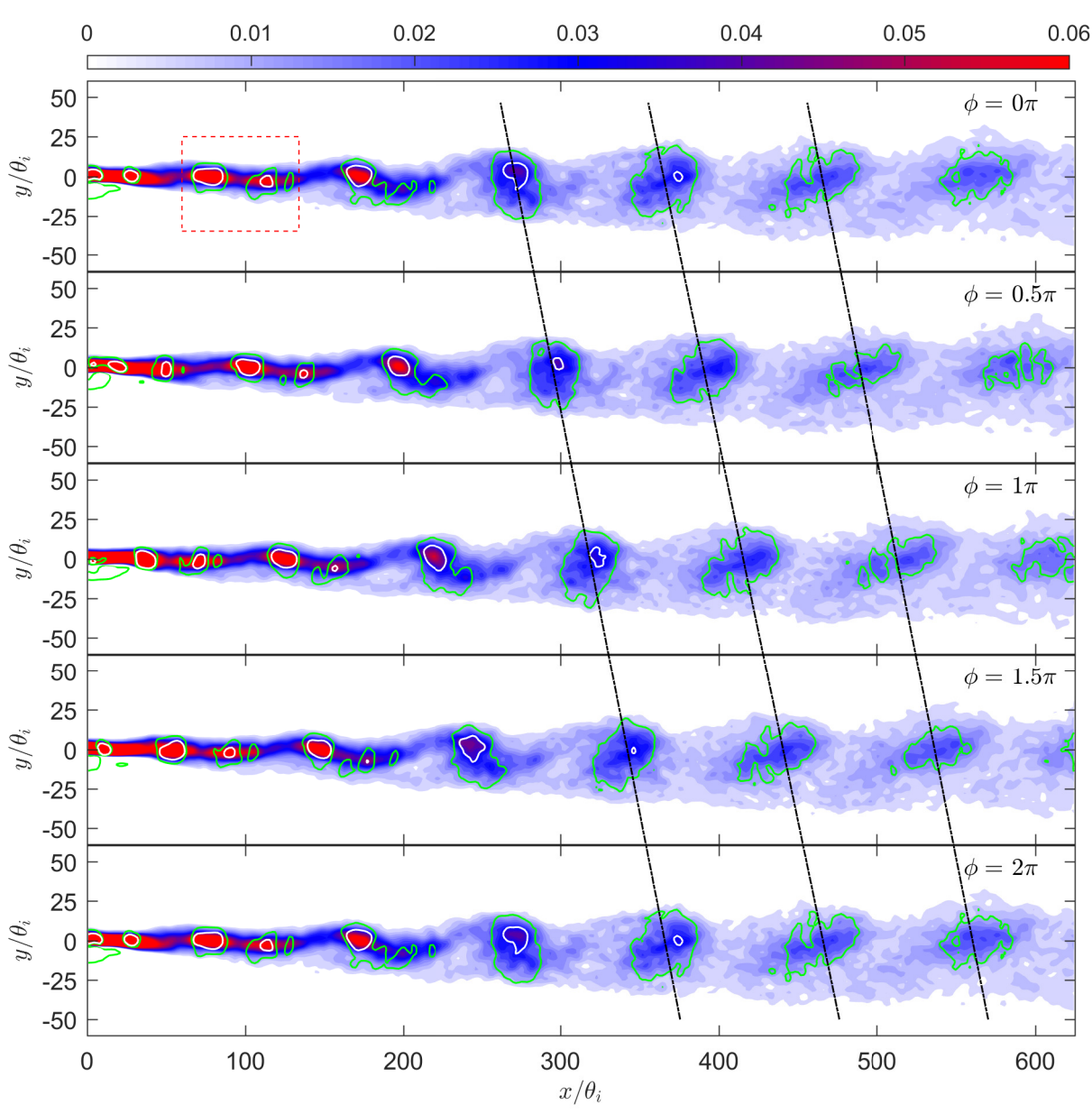
0
0.01
0.02
0.03
0.04
0.05
0.06
$\phi = 0\pi$
$\phi = 0.5\pi$
$\phi = 1\pi$
$\phi = 1.5\pi$
$\phi = 2\pi$
y/θ_i
50
25
0
-25
-50
0
100
200
300
400
500
600
x/θ_i

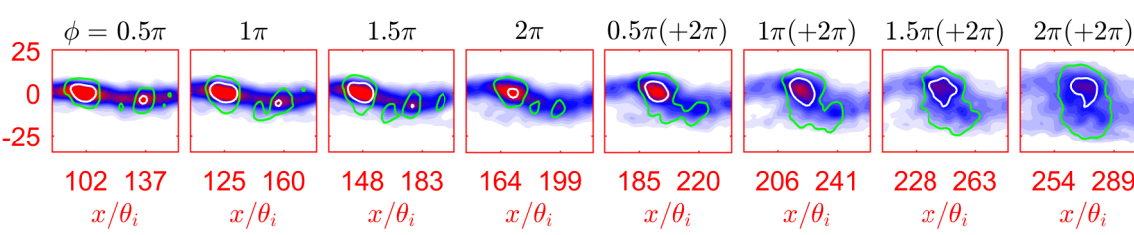
$\phi = 0.5\pi$
1π
1.5π
2π
$0.5\pi(+2\pi)$
$1\pi(+2\pi)$
$1.5\pi(+2\pi)$
$2\pi(+2\pi)$
y/θ_i
25
0
-25
102 137
125 160
148 183
164 199
185 220
206 241
228 263
254 289
x/θ_i